Construction and Building Materials 477 (2025) 141314

Contents lists available at ScienceDirect

Construction and Building Materials

journal homepage: www.elsevier.com/locate/conbuildmat

Intrinsic rheological behavior of limestone calcined clay cementitious (LC^3) binders for automated construction: Effect of calcium sulfate varieties

Mirza Abdul Basit Beigh [a], Cesare Signorini [a,*], Asim Rauf [a], Christof Schröfl [a], Thomas Köberle [a], Konrad Grahl [b], Thomas Matschei [b,c], Viktor Mechtcherine [a]

[a] Institute of Construction Materials, TU Dresden, Dresden 01062, Germany
[b] Building Materials Laboratory, HTW University of Applied Sciences, Dresden 01062, Germany
[c] Institute of Building Materials Research and Chair of Building Materials, RWTH Aachen University, Aachen 52062, Germany

ARTICLE INFO

Keywords:
Limestone calcined clay cement
Calcium sulfate
Rheology
Structural build-up
Hydration kinetics

ABSTRACT

As the concrete industry moves toward sustainable, automated construction, understanding the rheological behavior of alternative binders is essential. In particular, the rheology of limestone calcined clay cement (LC^3) is extremely sensitive to the type of calcium sulfate used. This study systematically investigates the impact of anhydrite ($CaSO_4$), bassanite ($CaSO_4{\cdot}0.5\ H_2O$), and gypsum ($CaSO_4{\cdot}2\ H_2O$) on hydration kinetics, structural build-up, and workability of LC^3 pastes. Isothermal calorimetry, rotational and oscillatory rheometry (Large-Amplitude Oscillatory Shear (LAOS) tests) were used to decouple the interplays between sulfate dissolution, hydration and thixotropic behavior. The results indicate that bassanite accelerates early-age structuration due to its rapid dissolution and ettringite formation, yielding a high structuration rate ($A_{thix} = 0.5$ Pa/min) and optimal shear stress evolution (up to 102 Pa). Conversely, gypsum retards structuration and extends workability beyond 140 minutes, but compromises early stiffening. Anhydrite, despite its coarser morphology, exhibited intermediate behavior with rapid workability reduction. LAOS analysis also identified distinct viscoelastic thresholds. Pastes with bassanite reached critical strain (10^{-3}) and crossover strain (10^{-2}) at minimal deformation, ideal for automated construction, while gypsum formulations showed delayed stiffening. This study demonstrates that sulfate selection directly controls open time, with bassanite formulations requiring a 90-minute operational time frame to balance extrudability and layer stability. These findings underscore the need to tailor calcium sulfate type to application-specific rheological demands and offer a pathway to optimize LC^3 binders for automated processes such as robotic shotcreting and 3D concrete printing.

1. Introduction

The construction industry is currently facing urgent challenges to improve sustainability, in particular to tackle the environmental impact of the massive production of concrete and cementitious materials. In this direction, advances in concrete technology, such as carbon capture, alternative materials, and efficient processing, are key areas of focus. Replacing Ordinary Portland Cement (OPC) with supplementary cementitious materials (SCMs) derived from industrial by-products (granulated blast-furnace slag, coal fly ash) [1] and natural ashes (e.g., rice husk and sugarcane bagasse ash) [2] offers a promising strategy to reduce CO_2 emissions by 5–8 % [3]. However, these sources can hardly meet the high demand of the construction industry for partial substitution of Portland cement clinker.

As an excellent alternative, natural SCM sources that are abundant worldwide are kaolinitic clays, which are characterized by exceptional pozzolanic reactivity after calcination [1,4]. The clays of interest do not need to feature high purity or high kaolinite content, as clays with a kaolinite contents above 40 % already have excellent pozzolanic reactivity and are good candidates for blended binders in concrete [5]. In addition, limestone powder is also considered an appropriate SCM due to its high availability, low production costs and low energy consumption [6]. Notably, limestone powder adjusts the particle size distribution (PSD) of the binder system in the fine range, and is therefore able to control workability while improving early-stage strength [7–9]. Limestone also promotes hydration to a certain extent by providing suitable nucleation sites for hydrates (filler effect) and contributes to the hydration in the presence of the aluminate phase depending on the PSD

* Corresponding author.
E-mail address: cesare.signorini@tu-dresden.de (C. Signorini).

https://doi.org/10.1016/j.conbuildmat.2025.141314
Received 28 November 2024; Received in revised form 9 April 2025; Accepted 11 April 2025
Available online 19 April 2025

itself [9,10].

Over the past decade, the advantages of calcined clay and limestone have been combined to develop an innovative blended binder, commonly referred to as Limestone Calcined Clay Cement (LC^3) [11–13]. LC^3 typically consists of 50 % clinker, 30 % calcined clay, 15 % limestone, and 5 % calcium sulfate (or related hydrates) [13] and have recently emerged as an up-and-coming alternative for the production of high-performance, sustainable cement-bonded construction composites [14–16]. As a result, extensive research has been devoted to the further development of this cutting-edge concept [17–20]. Most remarkably, the dosage of calcium sulfate, albeit low (on average 5 % by weight), plays a crucial role in the microstructural development of LC^3 binders. Indeed, it has been observed that LC^3 requires an additional amount of sulfate, beyond what is present in the OPC to attain robust performance [19,21]. Zunino et al. [9] demonstrated that the increased surface area provided by SCMs, rather than alumina content, drives the higher sulfate demand in LC^3. Sulfate is initially adsorbed onto C-S-H phases during the rise to the alite (C_3S) peak, accelerating C-S-H precipitation and leading to early gypsum depletion. As sulfate desorbs, it reacts with aluminates to form ettringite, creating a nanocrystal network that promotes early setting [22]. If the formulation is not adjusted to the appropriate sulfate dosage, the aluminate peak will occur before the alite peak in calorimetric analyses, hampering the strength gain of the system [23].

The need for calcium sulfate adjustment is also highlighted for other blended binders where cement is mixed with other phases (e.g., industrial or natural ash, calcined clay, silica fume) [24–27]. The primary objective of adding calcium sulfate to OPC or blended cements is to control the reaction kinetics of tricalcium aluminate (C_3A) to inhibit flash-setting [28]. In the case of blended cements containing calcined clay the proportion of calcium sulfate is typically set at around 5 % and plays a significant role in improving strength and durability. Zunino et al. [9,29] have nicely argued the importance of a well-sulfated system of LC^3 binder system to achieve optimum performance. Indeed, undersulfation may result in loss of strength due to the aluminate peak overriding the silicate peak, while oversulfation can cause a significant delay in the occurrence of the aluminate reaction peak [30].

In the blended cement system, a linear relationship was observed between the SO_3 content and the heat released up to the onset of the aluminate peak [28]. However, the mechanism by which calcium sulfate slows the reaction of C_3A is still a matter of debate. In this regard, recent studies challenge the standard textbook view that ettringite forms a diffusion barrier [31–33]. C_3A reacts instantly with water and rapid setting can occur by the formation of crystalline hydrates such as C_3AH_6, C_4AH_{19} and C_2AH_8, rendering the mixture unusable due to its high viscosity and low workability. In this respect, calcium sulfate acts as a setting retarder by forming ettringite. Zunino and coauthors [29,34] showed that the increased sulfate requirement of LC^3 vs. OPC results from the enhanced alite reaction driven by the filler effect and sulfate adsorption in C-A-S-H rather than the aluminate content of the calcined clay. These studies clearly highlight the key role of calcium sulfate in blended cements. However, they also leave significant knowledge gaps. While discussing the concepts of hydration products formation, it is essential to correlate them with the fresh state properties of advanced binder systems to ensure adequate workability, especially in the direction of developing automated construction technologies. The rheological performance of LC^3 systems for 3D concrete printing has previously been explored in the literature [35–38]. These studies provide relevant benchmarks for evaluating rheological performance and structuration characteristics of LC^3 binders although they do not explicitly delve into the implications of using different calcium sulfate sources. This emphasizes the need for a detailed study of the rheological properties, especially yield stress and viscosity, of LC^3 with various calcium sulfate types in order to refine these new binders for practical applications [39,40]. On the other hand, some recent research addresses the effects of different calcium sulfate varieties on hydration and flowability of cementitious binders [41,42] and corresponding concrete formulations based on OPC [43]. However, neither the state-of-the-art summary by Sharma et al. [44] nor the review by RILEM Technical Committee 282-CCL [45] have emphasized such a need for research for more complex blended binders such as LC^3. Muzenda et al. [46] used Large Amplitude Oscillatory Shear (LAOS) to study the rheology of LC^3 binders. They found that calcined clay increases static and dynamic yield stress, thixotropy, plastic viscosity, and cohesion while reducing harmonic distortion, whereas limestone has the opposite effect. Ferreiro et al. [47] further examined LC^3 rheology and found workability highly dependent on calcined clay content, especially with kaolinite. LAOS offers distinct insights into rheology for automated applications like 3D printing by identifying material responses to small deformations, capturing flow onset accurately [48]. It is a suitable technique to characterize the rheological behavior of such dynamic SCMs, in particular, an estimation of the open time can be achieved. Indeed, LAOS can distinctively identify the response of the material to certain deformation at very small strain levels, which are generally not apparent to normal observation, and then provide a detailed information on the deformation that leads to the visible flow i.e., the cross over [46,49–51]. Systematically linking flow values and rheological indices is key to comprehensively understanding the rheological behavior of concrete for advanced automated applications [52].

Research into the rheological behavior of LC^3 blended binders is still in its early stages and is evolving as the technology advances. This article is intended as a first step in addressing a critical knowledge gap by examining how different types of calcium sulfate affect the rheological properties of LC^3 binders, with the goal of designing high-performance composites for automated construction, with properties suitable for 3D printing and robotic shotcrete. For the ease of material availability and accessibility, only commercially available substances have been used. Instead of starting from a Portland cement clinker, a ready-mixed Portland cement CEM I was used in this study, accepting its calcium sulfate content and types. Robust testing methods and accurate data processing protocols are emphasized to support this investigation.

2. Experimental program

2.1. Formulation of the binders and raw materials

Three LC^3 pastes were designed to feature a nominal degree of OPC substitution by 50 %. A paste containing fly ash (reactivity parameter $k = 0.4$) as the sole SCM replacing OPC is considered as a benchmark and is referred to as M1-FA [53]. Although this formulation has a higher replacement level (55 %), as a result of appropriate workability adjustments, it is here considered a benchmark with an established SCM. While a direct comparison with M1-FA is not possible due to the slightly different proportions in the binder blends and in the solid/liquid ratio, the results are provided to establish a qualitative benchmark, while a direct quantitative comparison is deemed appropriate only among the LC^3 blends. All binder compositions are listed in Table 1 along with the commercial names and suppliers of the raw constituents.

A quite high dosage of polycarboxylate-type high-range water reducing admixture (HRWRA), with an active agent content of 39.5 % in the stock solution, ensures sufficient workability, i.e., flowability. The resulting water-to-binder (w/b) ratio, including the water from the HRWRA, is 0.3, according to EN 206–1/EN 1045–2. The fly ash-based binder contains a chemical stabilizer to stabilize the rheology in the fresh state. It consists of a cellulose ether matrix with calcium carbonate as a mineral additive. A Hägermann flow table was used to qualitatively control the spread diameter of the free-flowing paste, extending the common procedure in the EN 1015–3 that is typically restricted to mortars. This preliminary check was functional to slightly adjust the pastes to obtain a similar slump flow spread diameter, thereby ensuring a proper comparison. The HRWRA dosage over the sum of solid constituents is 0.97 % for M1-FA, 0.92 % by the weight of binder for the LC^3 counterparts, except for M1 LC^3-D which required only 0.75 % to meet

Table 1
Mixture compositions (all dosages are given in kg/dm^3 of paste).

Constituent	Supplier	M1 FA	M1 LC^3-A	M1 LC^3-B	M1 LC^3-D
CEM I 52.5 R-SR3/NA	Holcim GmbH, DE	0.645	0.764	0.764	0.764
Fly ash	Steament H−4, STEAG Power Minerals GmbH, DE	0.791	-	-	-
Limestone	Saxodol® 90 L.E., SH-Minerals GmbH, DE	-	0.242	0.242	0.242
Calcined clay	Liapor GmbH & Co.KG., DE	-	0.483	0.483	0.483
Calcium sulfate*	see Table 2	-	0.038	0.038	0.038
Water	Local tap water in Dresden, DE	0.435	0.458	0.458	0.458
HRWRA**	Glenium ACE 460, BASF, DE	0.014	0.014	0.014	0.011
Stabilizer	UW Compound−100®, Sika, CH	0.002	-	-	-

* = Three different calcium sulfate varieties (A, B and D), see Table 2.
** = High-range water reducing admixture

the target flowability criteria.

The LC^3 compositions investigated in this study are designated M1 LC^3-A, where LC^3 contains anhydrite, and similarly, M1 LC^3-B and M1 LC^3-D, where hemihydrate/bassanite and dihydrate/gypsum are used as sulfate carriers, respectively. The grades and properties of the calcium sulfates are reported in Table 2.

Since the gain in the structural build-up in the calcined clay-based mixes is significantly higher than in the OPC-based counterparts, and undersulfation leads to a rapid loss of workability [54], LC^3 binders with 50 % OPC replacement require a certain amount of calcium sulfate, which is 5–6 % by mass of the total binder, as also substantiated by preliminary studies [29,55]. Considering the presence of calcium sulfate hemihydrate and gypsum in the cement that was used, the remaining 2.5 % of the sulfate was added to reach approximately 5–6 % in the mix design. However, previous studies have demonstrated that sulfate demand in LC^3 is not only influenced by molar concentration but also by dissolution kinetics and interaction with aluminates, which affect ettringite formation and setting behavior [29]. Differences in solubility between sulfate sources (gypsum > bassanite > anhydrite) and ettringite formation are also expected to play a role in early structuration and rheology. While this is recognized, the sulfate content was standardized based on 5–6 % SO_3 by binder mass to ensure consistency across the different sulfate sources. While molar mass variations exist among the different calcium sulfate phases (i.e., $CaSO_4{\cdot}2\ H_2O$, $CaSO_4{\cdot}0.5\ H_2O$, and $CaSO_4$) the adoption of a mass-based approach aligns with industrial dosing practices and maintains the same sulfate availability in practical applications. In addition, M1 LC^3-B including bassanite was developed in previous works where it served as the basis for the production of high-strength, strain-hardening cementitious composites reinforced with randomly dispersed short fibers [56–58].

2.2. Physical and morphological properties of the binder constituents

To characterize the cement, calcined clay, limestone, calcium sulfate, and its hydrates at hand, quantitative powder X-ray diffraction (Seifert 3003 TT, Freiberg, Germany) was carried out at 40 kV and 30 mA using Cu K_α radiation in the range of 5° to 70° 2θ. Data were collected using a step size of 0.02° and a counting time of 6 s. Rietveld refinement was performed using AutoQuan version 2.70. An internal standard of 10 % ZnO was mixed with the samples. The analytical results, i.e., the mineralogical composition of the raw materials using X-ray diffraction, are reported in Fig. 1 for the main binder constituents and in Table 3 specifically for the calcium sulfates.

It is noteworthy that the amorphous phase in the calcined clay is about 65 %, while a difference emerged in the purity grades of the calcium sulfates as reported by the suppliers in Table 2, compared to Table 3, obtained by in-house investigation using XRD.

The PSD of the constituents was measured using an LS 13 320 particle size laser analyzer (Beckman Coulter, Inc., USA). Related findings are plotted in Fig. 2. Table 4 presents the characteristic particle diameters. The d_{50} of cement is 7.4 μm and the cement particle sizes range from 1 μm to 30 μm. Interestingly, the d_{50} for calcium sulfate anhydrous (A) is 2.6 times higher than calcium sulfate hemihydrate (B) and 3.43 times higher than calcium sulfate dihydrate, indicating a comparatively coarser PSD. Since the particle sizes of the LC^3 components, especially calcium sulfate and limestone, are markedly higher than those of cement, they are unlikely to impair the fresh-state properties of the LC^3 blends compared to the reference mix [59,60].

The specific surface area (SSA) of the raw constituents was determined by air evacuation and nitrogen adsorption, employing the Brunauer-Emmett-Teller (BET) method (Sorptomatic Model 1990, Porotec GmbH, Germany). Samples of the raw materials (13 g) were dried and placed in the apparatus at 50 °C. The measurement was carried out at a relative pressure of $p/p_0 = 0.33$, 22 points were detected, and the evaluation of sorption isotherms and specific BET surface area was performed by the instrument software. The measurement time was approximately 100 minutes. It was found that the calcined clay features a SSA that is more than four times that of OPC and fly ash (see Table 5), causing the widely recognized increase in the water demand for LC^3 binders compared to plain OPC. The SSA, along with PSD, is anticipated to have a decisive effect on the rheological properties of the binder system [61,62].

It can be noted that, while the SSA of calcium sulfate A is higher than the other counterparts, it also has substantially coarser particles, suggesting the key role played by the intricate and widely cracked morphology of the anhydrous calcium sulfate, as evident in the polarized light and scanning electron microscopy images of Fig. 3.

2.3. Paste preparation for rheological investigation and isothermal calorimetry

A bench planetary mixer (type ZMM5, Otto Mondschein Maschinenbau, Meißen, Germany) was used to prepare the batches for rheological investigation. One liter of cement paste was prepared for each experiment according to the protocol reported in Table 6. All pastes underwent the same shear history. Water was quickly added to the dry

Table 2
Chemical formulation, producer, and source of origin of calcium sulfates under investigation.

Calcium sulfate	Label	Chemical formula	Supplier	Country	Mol. Wt. [g/mol]	CAS Nr.*
anhydrous, purity grade 99 % (*anhydrite*)	A	$CaSO_4$	Acros Organics	Spain	136.14	77778–18–9
hemihydrate (*bassanite*)	B	$CaSO_4 \cdot 0.5\ H_20$	Honeywell	Germany	145.15	10034–76–1
dihydrate (*gypsum*)	D	$CaSO_4 \cdot 2\ H_2O$	Grüssing	Germany	172.17	10101–41–4

CAS Nr*. defined as "*Chemical Abstracts Service Registry Number* (www.cas.org)"

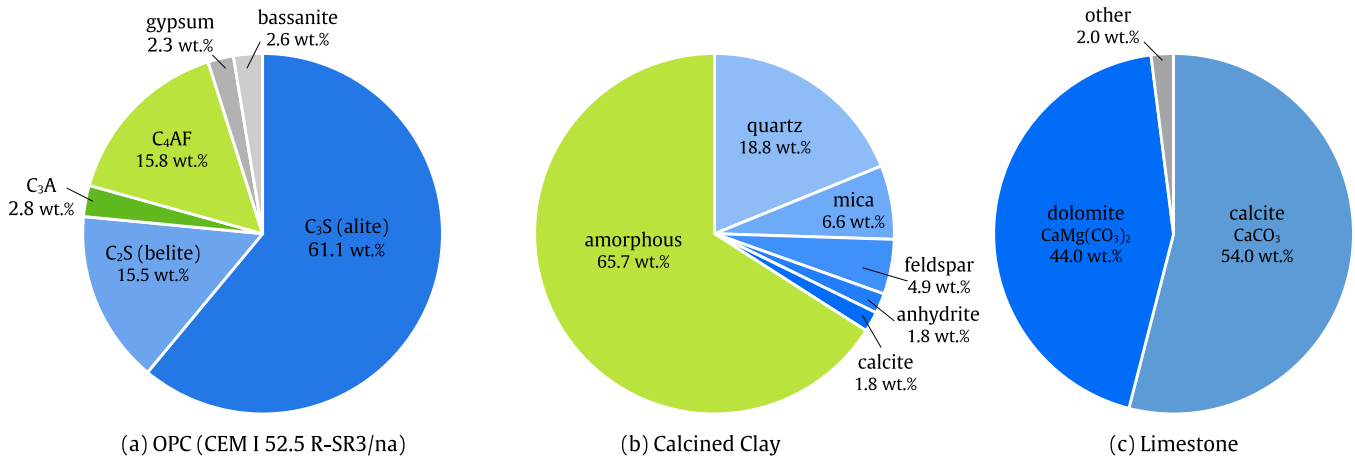

Fig. 1. Mineralogical composition of the main binder constituents [wt.-%].

Table 3
Mineralogical composition of the calcium sulfates under investigation, named as A, B, and D (according to the nomenclature in Table 2) and its hydrates as detected with XRD (all values are given in wt%).

Calcium sulfate type (cf. Table 2)	Hydrates and impurities according to XRD analysis				
	Anhydrite	Hemihydrate	Gypsum	Subtotal ($CaSO_4$)	Impurities *
A	83	17	-	100	-
B	-	100	-	100	-
D	6	-	91	97	3

* = Minor impurities: *calcite*.

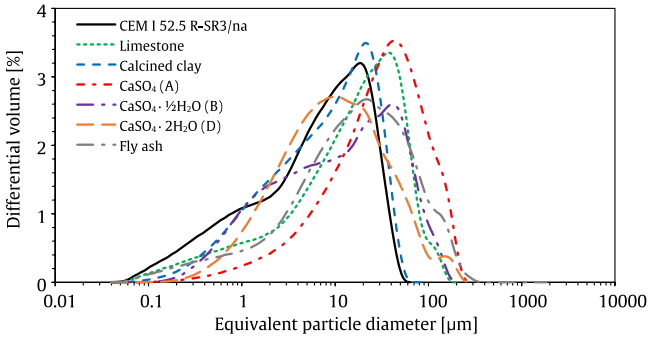

Fig. 2. Differential volumetric particle size distributions of cement, calcined clays, limestone, calcium sulfates, and fly ash (laser granulometry).

Table 4
Characteristic particle diameters of the powders as determined by laser diffraction.

Binder constituents	d_{10} [µm]	d_{50} [µm]	d_{90} [µm]
Cement	0.6	7.4	26.5
Fly ash	1.6	17.6	86.4
Limestone	1.2	17.8	59.6
Calcined clay	1.1	9.3	29.2
Calcium sulfate anhydrous (A)	4.9	33.3	112.7
Calcium sulfate hemihydrate (B)	1.2	12.7	63.9
Calcium sulfate dihydrate (D)	1.7	9.7	50.5

pre-blended powder, followed by thorough homogenization by mixing at increasing rotational speed. Practical laboratory experience suggests repeatedly that fast water addition is necessary.

In fact, too slow and gradual addition of water in many cases results in inhomogeneous dispersion, leading to clearly visible flocculation that cannot be overcome is successive steps of the mixing sequence. The mixed paste was poured into the unit cell for rheometry analyses in three stages to ensure that no air was entrapped.

2.4. Experimental methods

2.4.1. Isothermal calorimetry

Isothermal calorimetry of the binder systems was conducted at 20 °C using a CALMETRIX I-Cal Flex calorimeter (Boston, USA). Each ampoule contained 10 g of paste mixed with a vortex mixer at 800 rpm for 3 minutes. The first 45 minutes of data were excluded due to external mixing, and subsequent data were analyzed. The low water content prevented paste segregation, and measurements adhered to ASTM C1679, C563, C1702, and EN 196–11 standards.

2.4.2. Rotational rheometry

A coaxial rheometer Haake Mars II with a unit cell and vane rotor was used to investigate the rheological properties of the compositions (Fig. 4). Steel lamellas on the inner surface of the unit cell provide slip resistance. During the test, the temperature was kept constant at 20 °C. As the gap between the two cylinders is minimal, a constant shear rate can be assumed across the test samples.

To thoroughly characterize the rheology of the LC^3 pastes, compared to the FA benchmark, a preliminary hysteresis loop test was conducted to determine the Bingham properties. This was followed by a shear growth test to establish structural build-up parameters. Finally, oscillation rheological tests were conducted to ascertain the intrinsic rheological behavior.

2.4.2.1. Hysteresis loop. A preliminary hysteresis loop was performed 10 minutes after the addition of water. This loop was applied to ensure that the deflocculated state is achieved in the tested specimen, according to the reference state defined by Roussel [63], which also offers insights into the flocculation that occurs immediately after water addition, i.e., the *structuration rate*. To this end, a three-stage protocol similar to that of Nerella et al. [64] was implemented, consisting of a shear rate increasing from 0 to 4 s^{-1} over 30 s, followed by constant shearing at a rate of 4 s^{-1} for 60 s, and a final shear rate decreasing from 4 s^{-1} to 0 s^{-1} over the next 30 s. The typical output curve for the hysteresis loop is depicted in Fig. 5. The slope of the descending branch (no. 3) conventionally defines the Bingham plastic viscosity (μ) and the intercept of branch no. 3 on the *y*-axis represents the Bingham yield stress (τ). The specimen is kept at rest after the hysteresis loop is recorded.

Following the hysteresis loop test, two distinct test approaches were

Table 5
Specific surface areas of the powders under investigation [m^2/g] (BET method).

Cement	Fly ash	Limestone	Calcined clay	Calcium sulfate A	Calcium sulfate B	Calcium sulfate D
1.28	1.43	1.7	7.6	5.36	1.03	1.77

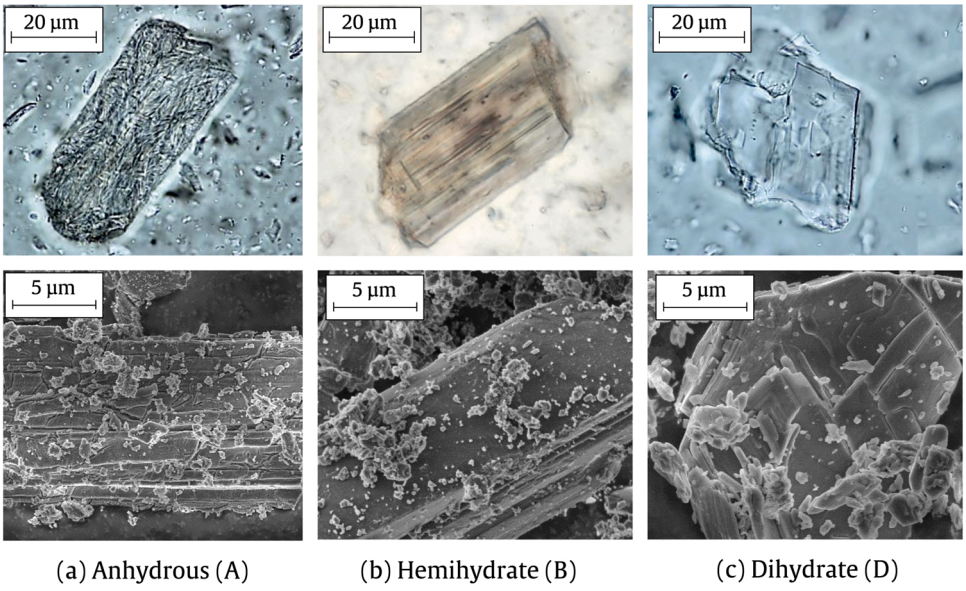

Fig. 3. Polar Light Microscopy (PLM, top) and Scanning Electron Microscopy (SEM, bottom) images of the calcium sulfate varieties, highlighting their distinctive morphology. The PLM images were taken in a Leitz Orthoplan Pol microscope, equipped with a Canon EOS 650D camera, while the field emission SEM images were taken in a QUANTA FEG 250 at 20 kV operating voltage and 40 Pa pressure.

Table 6
Mixing protocol of the pastes for rheological measurements.

Time [min: s]	Duration [min: s]	Speed [rpm]	Action
00:00 – 00:10	00:10	-	Adding water to the dry constituents
00:10 – 01:00	00:50	139	Mixing
01:00 – 02:30	01:30	-	Wall scraping
02:30 – 03:30	01:00	591	Mixing
03:30–04:00	00:30	-	Wall scraping
04:00 – 06:00	02:00	591	Final mixing

performed: stress growth and oscillation amplitude. A single batch was used for the former approach, while a multi-batch approach was adopted for the latter, as suggested in the literature [46,64,65].

2.4.2.2. Stress growth test. The primary objective of the shear stress growth test is to determine the maximum shear stress attained by the fresh pastes, which is considered the yield stress. Fig. 6a presents the typical shear strain and shear rate profiles during the tests and the expected experimental outcomes to extract the main parameters from this test. When visualizing stress development and apparent viscosity $\eta = \frac{\tau}{\dot{\gamma}}$, the shear stress rises to its maximum value as the deformation continues beyond the elastic domain, i.e., the linear range (Fig. 6b). The viscosity peaks (as marked by a vertical dashed line) occur when the shear stress deviates from the elastic domain, as visible by tracing the tangent straight line (plotted in red). Beyond this point, as the shear stress increases, the viscosity decreases to a minimum as the maximum shear stress is asymptotically reached, along with the viscosity minima (marked by the second vertical dashed line). The average values just after the end of the elastic domain are conventionally defined as the static yield stress.

The stress growth test is conducted at the sample ages t_{age} of 20, 40, 60, 100, and 140 minutes accounted from the time of water addition, applying a constant shear rate of 0.01 s^{-1} in accordance with previous studies [63,66–68]. The distinction between the applied shear rate and the effective shear rate of the rheometer has been outlined by Nerella et al. [64]. The stress growth test continues until the effective shear rate $\dot{\gamma}_{ef}$ approaches the applied shear rate $\dot{\gamma}_{ap}$ at which the maximum shear stress is attained [65]. Once the maximum shear stress is achieved the test automatically stops due to the break setting of the rheometer employed in the RheoWin software [65,69]. The testing profile is outlined in Table 7. Each test is repeated three times to ensure statistical reliability and reproducibility.

2.4.3. Oscillation rheometry: Large Amplitude Oscillation Shear (LAOS) technique

For a detailed characterization of the structural build-up in reactive cement-based materials, samples must be disturbed beyond their critical strain (yield stress), as required by automated techniques like 3D concrete printing. While rotational rheometry offers statistical reliability, it provides only instantaneous flow onset values and is somewhat destructive. To fully assess fresh-state properties, oscillatory rheometry is essential as it measures intrinsic behavior by quantifying critical strain and cross-over strain. Large Amplitude Oscillatory Shear (LAOS) has widely been utilized to evaluate the nonlinear viscoelastic properties of LC^3 systems, particularly in high-shear applications such as 3D concrete printing. Unlike traditional rheological methods, LAOS allows a deeper assessment of the strain-dependent thixotropic behavior, providing a more comprehensive evaluation of flow-induced microstructural changes during extrusion, providing crucial insight into structural breakdown and recovery mechanisms, which conventional yield stress or viscosity tests fail to capture [46,51,70].

This study uses amplitude oscillation strain sweeps to capture the following key parameters: storage modulus, loss modulus, complex viscosity, phase angle, and shear stress. In this way, structural build-up

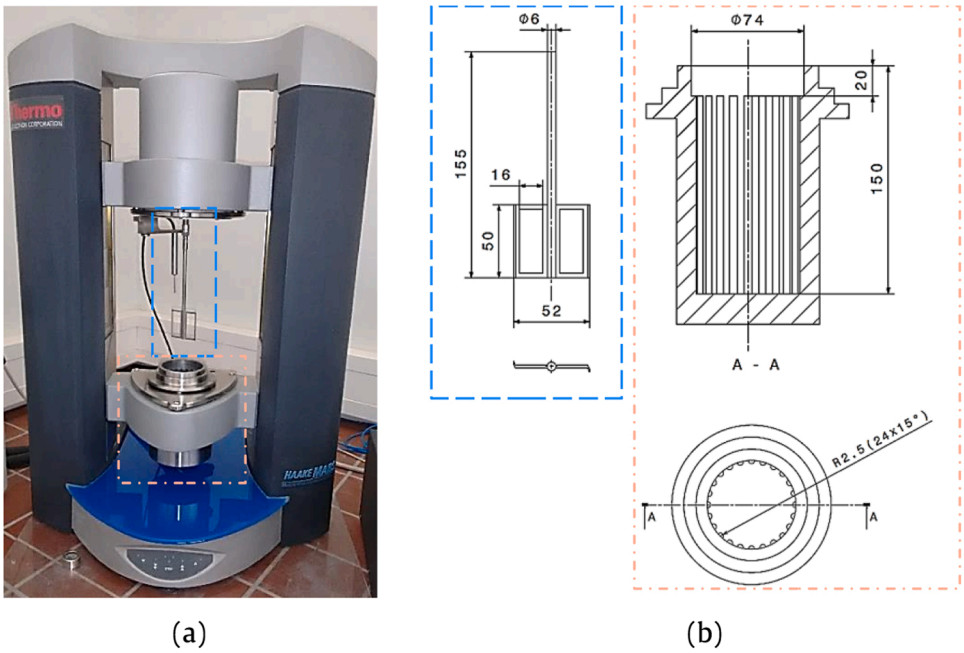

Fig. 4. Haake Mars II rheometer (a) and schematic of the unit-cell and (b) vane rotor (dimensions in mm).

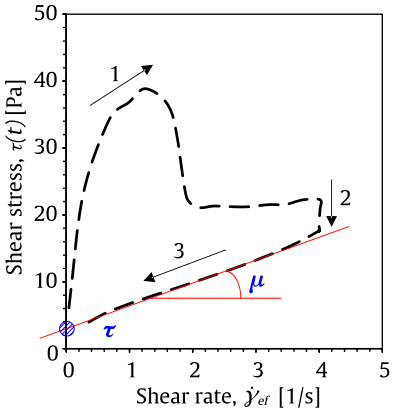

Fig. 5. Typical hysteresis loop output with the Bingham parameters indicated.

at a micro scale is mapped. By applying the LAOS technique to LC^3 pastes at various ages, using individual samples and triplicate testing, open time was estimated and rheological changes were tracked over

Table 7
Testing profile for assessing the structural build-up.

Stage	Relative time [min:s]	Applied shear rate [s^{-1}]	Action
Hysteresis loop	10:00 – 10:30	0 – 4	Shear rate up
	10:30 – 11:30	4	Constant shearing
	11:30 – 12:00	4 – 0	Shear rate down
Stress growth	20:00	0.01 < $\dot{\gamma}_{ap}$	
	40:00	0.01 < $\dot{\gamma}_{ap}$	
	60:00	0.01 < $\dot{\gamma}_{ap}$	
	100:00	0.01 < $\dot{\gamma}_{ap}$	
	140:00	0.01 < $\dot{\gamma}_{ap}$	

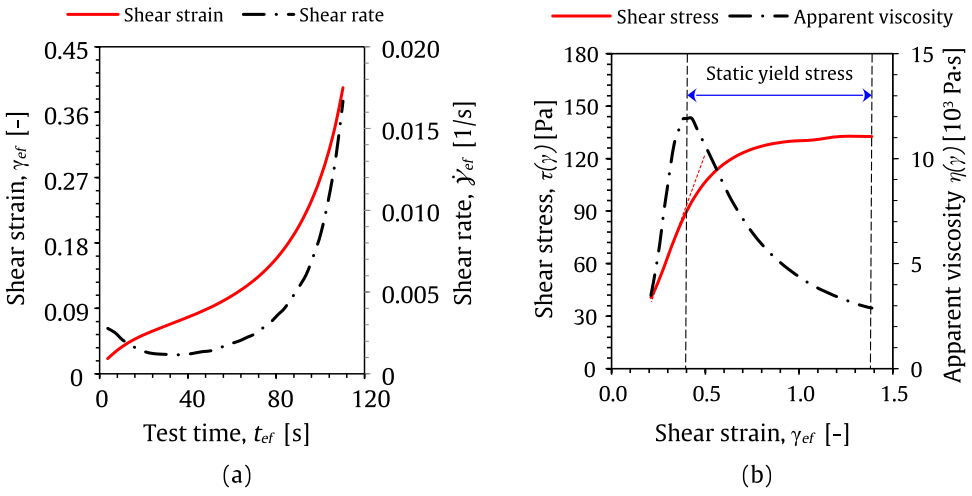

Fig. 6. (a) Typical effective shear strain and shear rate profiles versus test time, and (b) typical output in terms of shear stress and apparent viscosity versus shear strain. The dotted red line in the inlet *(b)* shows the linear trend of the shear stress. At the maximum viscosity, the shear stress deviates from the linear domain.

time to rigorously profile structural build-up.

The resistance of a specimen to the applied deformation is measured as the normalized shear stress. Since thee raw data appear as sinusoidal excitations (Fig. 7) they must be normalized using Fourier Transforms (FT). Shear stress and shear strain can be presented in terms of sine waves (raw data) using the following expressions:

$$\tau(t) = \tau_o \sin(\omega t) \quad (2)$$

$$\gamma(t) = \gamma_o \sin(\omega t + \delta) \quad (3)$$

where τ [Pa] represents the shear stress, γ the shear strain, ω the angular velocity, and δ the phase angle or the lag. The independent variable t represents the time history within the oscillatory cycle, measured in seconds (s).

The distinct feature of the oscillation amplitude strain sweep is its ability to utilize the complex moduli: the storage or elastic modulus (G') and the loss or viscous modulus (G") (unit: Pa). The absolute value of G*, denoted as |G*| (unit: $Pa{\cdot}s$), represents the total resistance against deformation and is used to calculate the complex viscosity |η*| (unit: $Pa{\cdot}s$). Elastic effects are in phase with the strain, while the viscous effects are in phase with the strain rate, defining G' and G''. In addition, a complex modulus is defined as $G^* = G' + iG''$ where i is the imaginary unit [71] (Eqs. 4 to 7).

$$G' = \frac{\tau_o}{\gamma_o}\sin(\delta) \quad (4)$$

$$G'' = \frac{\tau_o}{\gamma_o}\sin(\delta) \quad (5)$$

$$G^* = G' + iG'' \quad (6)$$

$$|\eta*| = \frac{|G^*|}{\omega} \quad (7)$$

As shown in Fig. 8, three different regions that describe the rheological behavior of viscous media can be identified: the linear viscoelastic region (LVR), the non-linear viscoelastic (so-called *transient*) region, and the cross-over stage. In the LVR, deformation occurs at the micro-level within the elastic domain, i.e., it is recoverable and does not induce dissipation, while the elastic and viscous moduli remain approximately invariant. When the micro-deformations exceed the elastic limit, the transition between LVR and the non-linear viscoelastic region occurs, defining the critical elastic shear strain and the corresponding elastic shear stress [72,73]. The non-linear region is characterized by a decreasing trend in the elastic and loss moduli, which account for elastic and viscous interactions. At a certain strain, G' and G"

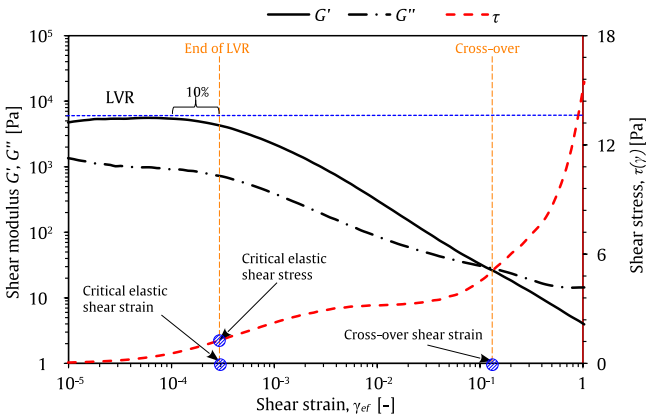

Fig. 8. Shear moduli (G', G'') and shear stress (τ) response to the effective shear strain applied to the specimen under investigation using LAOS, an example of a typical output.

tend to converge. This threshold is regarded to as the *cross-over strain*. Beyond this critical strain, the loss modulus dominates the elastic modulus, indicating that material is flowing [72–75].

The same Haake Mars II coaxial rheometer shown in Fig. 4 with RheoWin software was used for these tests. A multi-batch approach was adopted to avoid overestimation of the rheological properties due to cumulative deformation inside the sample, typical of the single-batch approach [65]. Strain amplitude sweeps ranged from 10^{-5} to 1 unit of strain. Initially, this amplitude sweep was applied at 140 minutes using a sweep frequency of 1 Hz to determine the critical strain. Data were processed according to DIN 51810–2, with a tolerance for LVR deviation of 10 % of the G' plateau value and considering a data tolerance of 5 % (Fig. 8).

A preliminary hysteresis loop was applied at the beginning of each test, i.e., 10 minutes after water addition. LAOS tests were then performed under a controlled shear strain regime by programming the rheometer with the "CD-Auto-strain" protocol. Tests were conducted at 20, 40, 60, 100, and 140 minutes after water addition, analogous to the stress growth method. The LAOS protocol starts 5 minutes before the target time because the strain of 10^{-5} units needs sufficient time to progress to the strain of 1 unit. During these 5 minutes, the material is perturbed in the linear viscoelastic region and the response lies in the elastic domain. This ensures an appropriate start of the test to capture the intrinsic behavior at the LVR boundary and the crossover without losing timely information. Data is collected in 100 steps, with each strain step repeated three times.

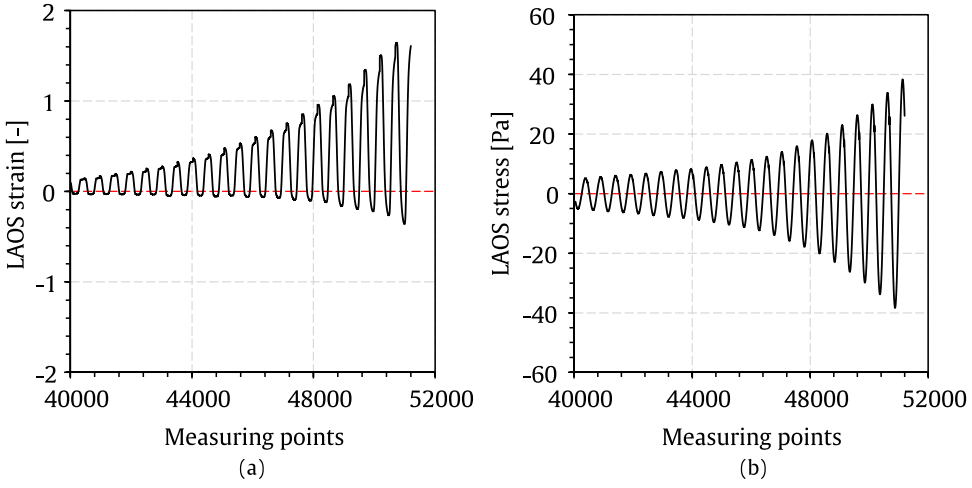

Fig. 7. (a) Shear strain excitation and (b) shear stress as a function of the measuring points (MPs).

2.4.4. Results interpretation

The structural build-up for LC^3 pastes as assessed using the rotational and oscillation rheometry is interpreted by fitting two established mathematical models of structural build-up, namely those developed by Roussel [68] and Perrot et al. [76] (Eqs. 8 and 9). These models describe the structuration rate of the suspension, a crucial parameter in advanced applications like shotcrete and 3D printing.

$$\textbf{Roussel's model}\ \tau_0(t) = \tau_0 + \tau_0\frac{t}{T} = \tau_0 + A_{thix}.t \quad (8)$$

$$\textbf{Perrot's model}\ \tau_0(t_{rest}) = \tau_{0,0} + A_{thix}.t_c(e^{t_{rest}/t_c} - 1) \quad (9)$$

In Eqs. 8 and 9, $\tau_{0,0}$ represents the static yield stress at the beginning of the rest period, t_c is the characteristic time, t_{rest} is the resting time, and A_{thix} is the structuration parameter. This structuration parameter encapsulates the thixotropy due to flocculation and hydration, offering a comprehensive view that accurately describes the time history of the rheological behavior. The static yield stress in the case of oscillatory rheometry is defined at the first critical and cross-over strain. These two strains are crucial and the corresponding static yield stress is plotted against time as discussed in Section 3.3. The complex viscosity $|\eta^*|$ and the complex moduli (G' and G'') are also plotted against time, with the results for both strain states discussed in Section 3.3. Leveraging the capabilities of LAOS, the structuration rate is defined as $A_{thix,elastic}$ and $A_{thix,cross\text{-}over}$ for the critical and cross-over strains, respectively. To the best of the authors' knowledge, the approach of decoupling structuration rates based on the viscoelastic behavior of cement-based materials had not been discussed prior to this work.

3. Results and discussion

3.1. Isothermal calorimetry

Fig. 9a presents the hydration rate and cumulative heat of hydration over the first 72 hours after water addition. The curves reveal that the dormant period for the LC^3 mixtures differs notably from that of the M1-FA mixture. The average dormant period for M1-FA is around 20 hours, nearly twice as long as for the LC^3 binders.

In the absence of any other analytical technique, this could be related to the combined addition of PCE and stabilizer. In fact, the HRWRA dosage over the sum of solid constituents is the highest for M1-FA (0.97 %), exceeding that of the LC^3 counterparts, namely 0.92 % for M1 LC^3-A and M1 LC^3-B and 0.72 % for M1 LC3-D. Furthermore, it should be noted that water-to-cement ratio is significantly higher for M1-FA (0.674) compared to that of LC^3 binders (0.599), leading to a probable delay in the formation of hydration products in M1-FA. As a matter of fact, the effects of PCE HRWRA and other additives in affecting the hydration kinetics are well documented [25,26]. Alternatively, in the presence of fly ash, the alumina concentration in the pore solution is increased, which restrains alite hydration, but does not retard overall hydration [24,25]. Regarding LC^3 pastes the three calcium sulfate types lead to characteristic effects on hydration. M1 LC^3-A exhibits the shortest dormant period of approximately 9 hours (see Fig. 9b), possibly attributed to the specific surface effect, while M1 LC^3-D has the longest, with around 12 hours. M1 LC^3-B demonstrates a mid-way behavior of around 10 hours. The trend in heat release during the dormant period mirrors the cumulative heat released. M1-FA records the lowest heat release compared to all LC^3 mixtures [25,26].

In addition, the alite (C_3S) peak for sulfate A occurs earlier than for B, which slightly precedes the alite peak of D. The expected occurrence of aluminate peaks after sulfate depletion cannot be clearly observed. This is probably due to the lower C_3A cement chosen. However, the derivative plotted in the inlets *c.1* to *c.3* of Fig. 9 shows a point of inflection, underlying a consistent trend. Notably, calcium sulfate D appears to exhibit a slightly higher hydration rate, as evidenced by a slightly elevated alite peak. M1 LC^3-D surpasses M1 LC^3-B after 21 hours. Several studies showed that calcined clay limestone cements are highly sensitive to the optimum sulfate content [6,19,29,77,78]. Recently, Zunino [29] showed that accelerated formation of C-A-S-H in LC^3 leads to an increased sulfate sorption on the available C-A-S-H surfaces. This may result in higher sulfate demand and faster sulfate carrier depletion. Since our cement contains only small amounts of C_3A, a distinct sulfate depletion peak is barely visible in the calorimetric measurement. However, as shown by the inlets in Fig. 9, the peak of the plot, the derivative of the power per gram of cement versus time, appears after the central alite hydration peak, but with a considerable delay and an indistinct appearance [55]. This indicates that our systems are either over-sulfated or that there is less reactive aluminate or less quantity of required aluminate in the blended cement [9]. The substantial delay in the hydration of the fly ash mix is not related to the sulfate content, but is probably caused by some interactions between the two admixtures, i.e., the PCE HRWRA and the stabilizer, also in conjunction with the binder composition used.

The dissolution behavior of calcium sulfates in LC^3 pastes is

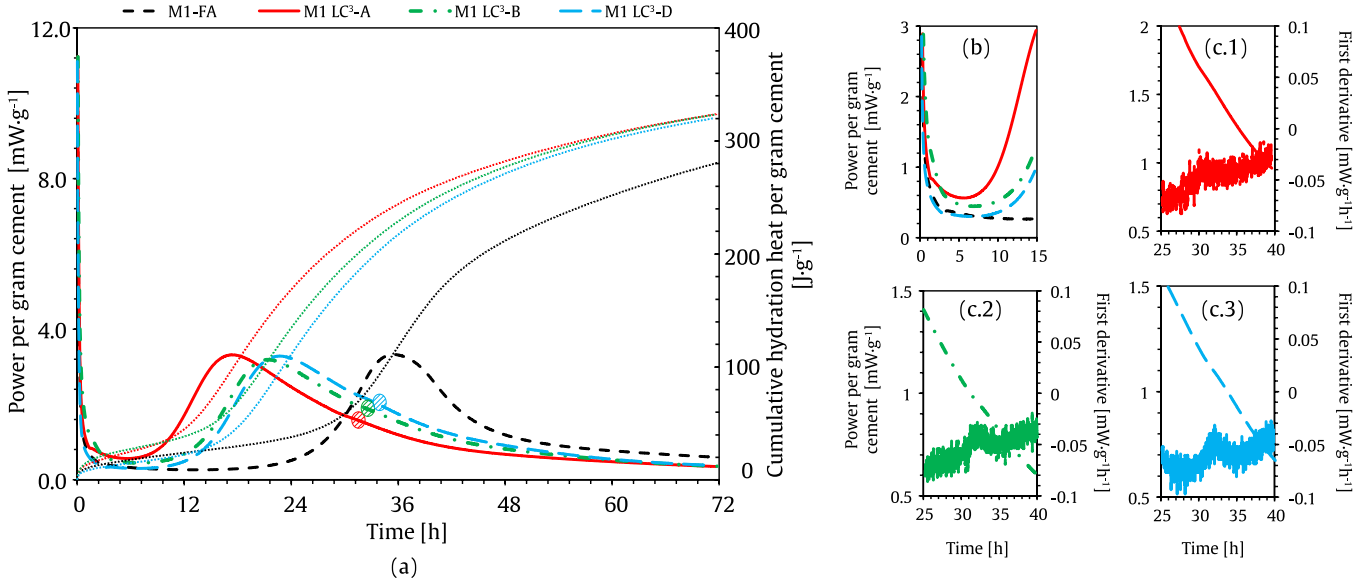

Fig. 9. Isothermal calorimetry data of LC^3-blended mixtures showing a close-up of the derivative of power from 25 to 40 hours of reaction time for calcium sulfate.

governed by a complex interplay between the physical and morphological properties of the constituents, namely their particle size and specific surface area. The calorimetric data in Fig. 9 show that the LC^3 binder containing anhydrite ($CaSO_4$, A) exhibits an earlier and more pronounced sulfate release than expected on the basis of its coarse particle size distribution (d_{50} = 33.3 μm, Table 4). On the other hand, this deviation from typical dissolution trends can also be attributed to its high SSA (5.36 m^2/g, Table 5). The extensive microcracking and fractured surface morphology, as observed in the micrographs in Fig. 3, increases the reactive surface area which is accessible to solvent and allows for dissolution of ions. In fact, such an enhanced contact area for water facilitates a more rapid release of sulfate ions, even though the particles themselves are rather coarse. In contrast, bassanite ($CaSO_4$·0.5 H_2O, B), despite having a finer PSD (d_{50}=12.7 μm) and a much lower SSA (1.03 m^2/g), leads to a slightly delayed response, likely due to its more compact, less fractured morphology which limits immediate dissolution. Calcium sulfate dihydrate ($CaSO_4$·2 H_2O, D) dissolves more slowly due to its stable crystalline structure and lower SSA (1.77 m^2/g), contributing to extended sulfate availability over time, which is consistent with its observed effect on extended workability windows as shown in the following sections. The study of the hydration kinetics of LC^3 pastes containing different varieties of calcium sulfate, from the dormant period to the acceleration and deceleration stages, has been scarcely explored in the existing literature. Krishnan et al. [27] applied isothermal calorimetry to LC^3 with different gypsum contents but did not vary the calcium sulfate type, while Chen et al. [79] used complementary analytical techniques similar to the present study (i.e. advanced rheological tests and isothermal calorimetry) but again considered only gypsum as the calcium sulfate species. Thus, the understanding gained in this study can provide a sound basis for elucidating the rheological properties and may ultimately provide critical insight into the mechanical behavior of LC^3-based materials in their hardened state. The rheological response in the following sections further supports these trends, with anhydrite-based LC^3 pastes exhibiting a high rate of early structuration (A_{thix}), lending credibility to the hypothesis that the fractured morphology of anhydrite accelerates sulfate release and promotes early ettringite formation and thus structuration. These findings underscore that sulfate dissolution kinetics in LC^3 systems cannot be solely inferred from PSD but require a combined evaluation of SSA, morphology, and microstructural defects, which collectively dictate sulfate availability, hydration kinetics, and rheological evolution.

3.2. Rotational rheology

3.2.1. Hysteresis loop and Bingham parameters

Fig. 10 presents the typical shear stress vs. shear rate curves obtained from hysteresis loop tests used to compute the Bingham parameters and structuration rates. The latter serves as an indicator of the structural build-up of the paste. It is computed as the area enclosed by the loop using the established Simpson's numerical integration rule (see Atkinson [80], Eq. 5.1.15).

The Bingham yield parameters obtained by the linear interpolation of the descending $\tau - \dot{\gamma}_{ef}$ curve (refer to branch no. 3 in Fig. 5) are compared in the bar charts of Fig. 11. M1 LC^3-A exhibits the highest structuration rate, followed by M1-FA (-26 %), M1 LC^3-B (-36 %), and M1 LC^3-D (-96 %). On the contrary, the reference paste M1-FA shows the highest values of Bingham yield stress and plastic viscosity, which is further confirmed and discussed in the subsequent sections.

Within the LC^3 binder systems, M1 LC^3-A had higher values of the Bingham parameters, followed by M1 LC^3-B and M1 LC^3-D in that order, with a similar trend for yield stress and plastic viscosity. The coefficient of variance (CoV) related to the Bingham parameters is less than 5 %, highlighting the good reproducibility of the measurements.

The result of the hysteresis loop demonstrates a distinct structuration rate of LC^3 binders compared to M1-FA at a very early age, a discrepancy also suggested by the apparent differences in the specific surface areas of the powders (see Table 5). Since the Bingham parameters are derived by extrapolating the descending branch of the loop to the y-axis, oversimplification may bias the results due to a notable non-linear behavior visible at the end of the descending branch between shear rate of 1 s^{-1} and 0 s^{-1}, unlike the LC^3 counterparts. The non-linear behavior observed in the descending curve of M1-FA may indicate transient structuring effects during flow where particle-particle interactions temporarily increase the shear resistance.

3.2.2. Stress growth test and structural build-up assessment

To illustrate the structural build-up of the pastes based on the stress growth test protocol, Fig. 12 and Fig. 13 plot shear stress and apparent viscosity, respectively, against the shear strain. All pastes consistently exhibit a monotonic increasing trend in the shear stress over time, correlated with the shearing applied to the specimen. At the same time, an increasing trend can be observed for the apparent viscosity. The shear stress growth at 20, 40, and 60 minutes is not well-defined for M1 LC^3-A and M1 LC^3-B. This phenomenon may result from multiple factors such as release of water molecules or intercalated superplasticizer from the calcined clay layered structure or some underlying chemical reactions.

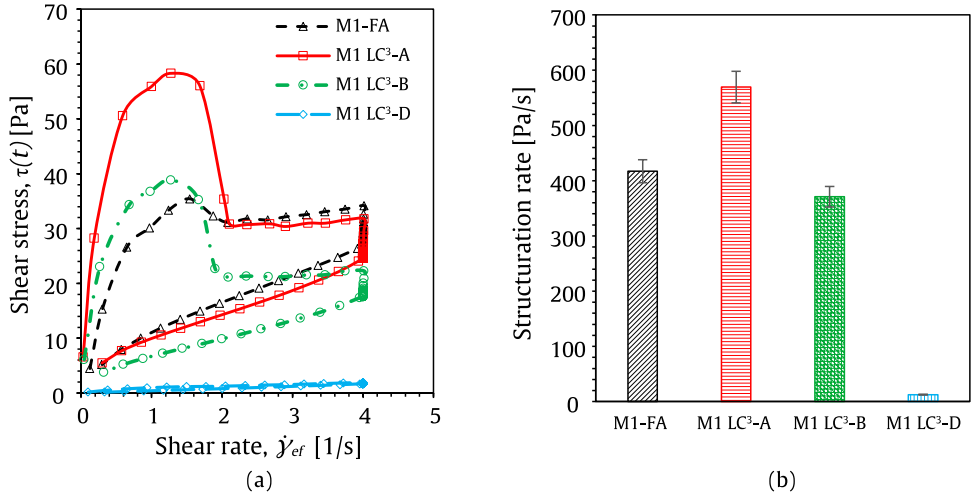

Fig. 10. (a) Hysteresis loops show shear stress as a function of the shear rate; (b) the area enclosed by the loops denoting the structuration rate of all pastes under investigation. Hysteresis loops were recorded 10 minutes after the addition of water.

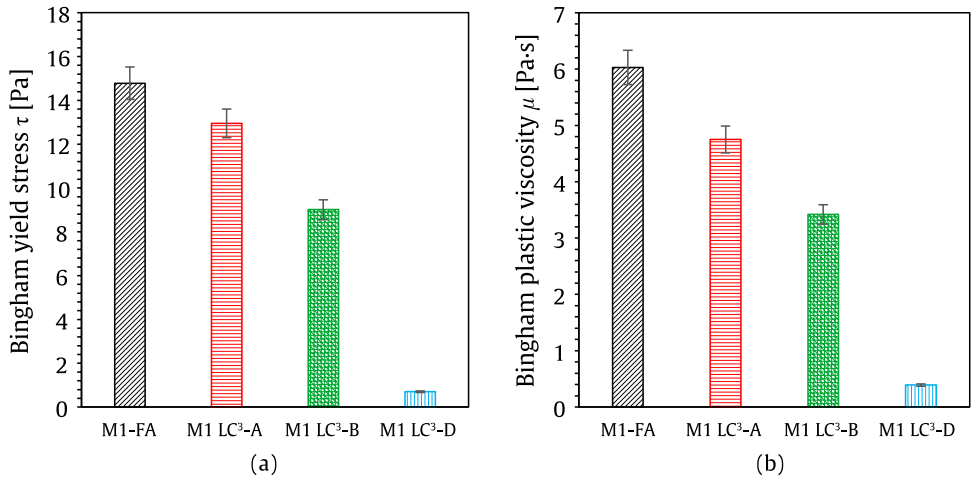

Fig. 11. (a) Bingham yield stress and (b) Bingham plastic viscosity of the pastes.

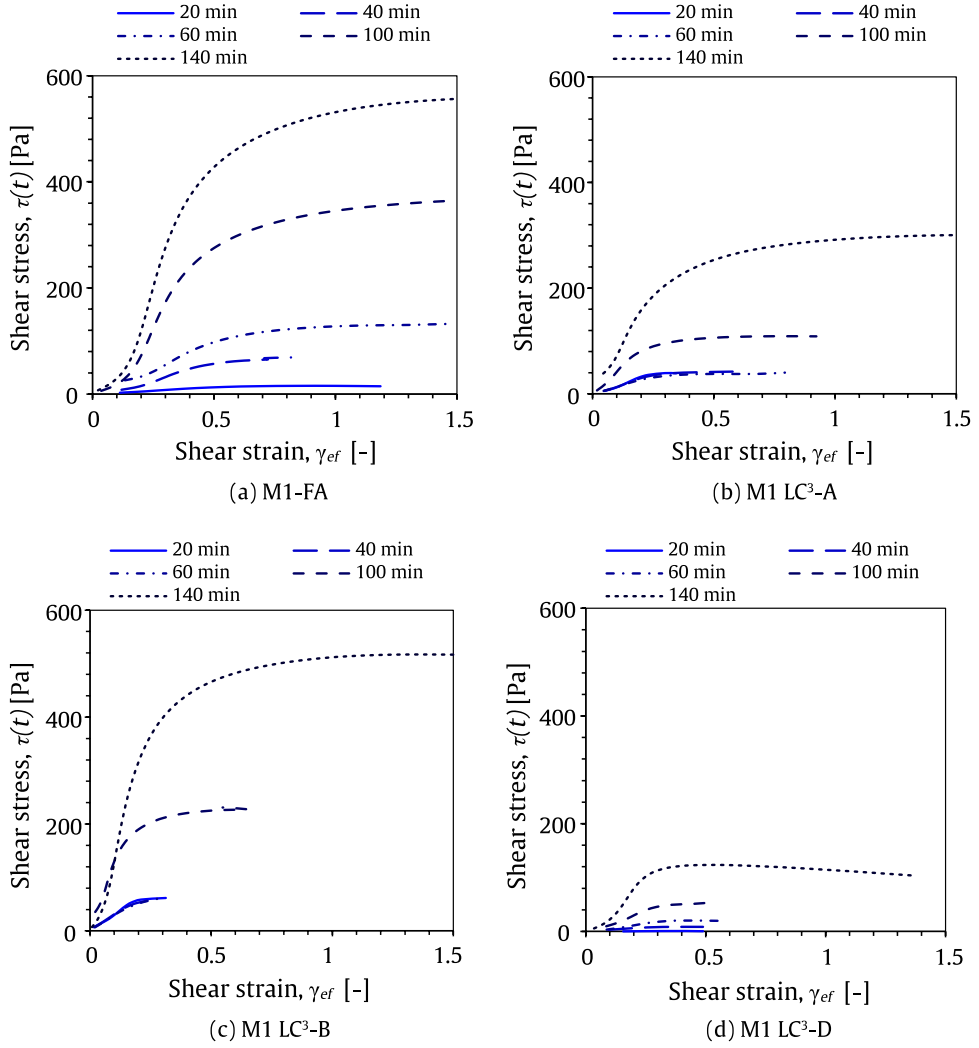

Fig. 12. Shear stress versus shear strain curves for all pastes under investigation.

However, the precise cause needs further investigation and should be addressed in subsequent studies.

Based on previous findings, M1 LC^3-D has the least structural build-up (see the inlets *d* in Fig. 12 and Fig. 13). Among the LC^3-based pastes, M1 LC^3-B has the highest structural build-up and apparent viscosity evolution over time. The results concerning apparent viscosity for M1 LC^3-A and M1-LC^3-B display discrepancies at 20, 40, and 60 minutes of age, which warrant further investigation in future studies.

Fig. 14 presents the static yield stress and corresponding apparent viscosity over time for each paste along with the mean values of the

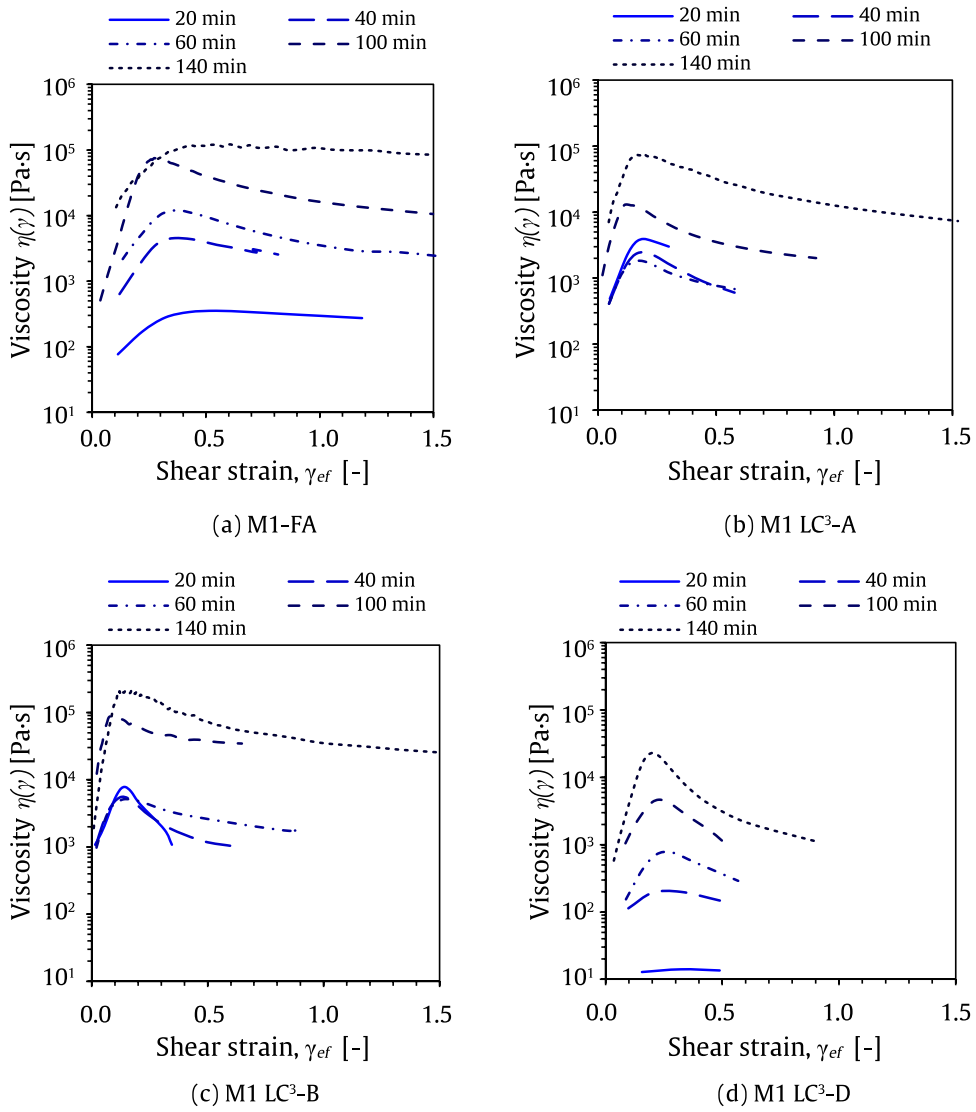

Fig. 13. Apparent viscosity versus shear strain curves for all pastes under investigation.

structuration rate A_{thix} measured accordingly. As shown in Fig. 14c, M1-FA has a notably high structuration rate. It is 2.6 times higher than M1 LC^3-A, 1.5 times higher than M1 LC^3-B, and five times higher than M1 LC^3-D. These findings are consistent with previous observations.

In terms of apparent viscosity, M1 LC^3-D demonstrates the lowest viscosity of the four mixes over time. However, it exhibits a steady increase akin to the reference paste M1-FA (Fig. 14b). Likewise, M1 LC^3-A and M1 LC^3-B show, to a lesser extent, a marginal loss in apparent viscosity at 40 and 60 minutes after water addition. However, these blends show a considerable increase in viscosity at 100 minutes and beyond.

A similar trend can be observed in Fig. 14a, which details the static yield stress. At the 20 minutes mark the apparent viscosity and shear stress of M1-FA are lower than the corresponding values for M1 LC^3-A and M1 LC^3-B, contrasting with the results of the thixotropic loop test. Again, the delayed formation of hydration products that was observed for M1-FA could be explained by the higher plasticizer dosage and w/c ratio, compared to that of LC^3 counterparts. Interestingly, the apparent viscosities of M1-FA and M1 LC^3-B exhibit a comparable temporal evolution, while their static yield stress varies significantly, indicating a possible correlation with the specific non-linear behavior observed in the hysteresis loop in Section 3.2.1. Further investigation is required to determine the exact cause of this unique behavior. Moreover, the impact of the different calcium sulfate varieties on the structuration rates of LC^3 pastes is quite noticeable. While the hysteresis loop test (Section 3.2.1) suggests that the initial structuration rate of mixture M1 LC^3-A is higher, M1 LC^3-B overtakes it over time. Conversely, the crystallization water of the gypsum in M1 LC^3-D possibly consumed less water for ettringite formation. This way, free H_2O molecules are provided to the system, which may suppress the structuration rate. However, in terms of the mass balance, this change must be marginal and should be further investigated [81,82]. During the initial hydration, there still needs clarity on which particular chemical reaction controls the flow behavior, especially in the first two hours after water addition. Roussel et al. [71] mention that the beginning of hydration on the rheology is primarily influenced by the silicate reaction, particularly by the precipitation of C–S–H. Therefore, correlating the structural build-up to the hydration of calcium sulfates and its hydrates needs more investigation. Jakob et al. [83,84] emphasize that the aluminate reaction dominates the hydration kinetics during the initial and induction periods. Jakob et al. [83,84] also suggest that ettringite formation leads to tangible changes in the water-to-solid ratio, the surface area, and the solid volume fraction.

A very important point of discussion is the water demand of LC^3 pastes that is primarily governed by the specific surface area and particle size distribution of its constituents. As shown in Table 5, calcined clay exhibits a much higher SSA (7.6 m^2/g) compared to other components, contributing to an increased water demand. The SSA of

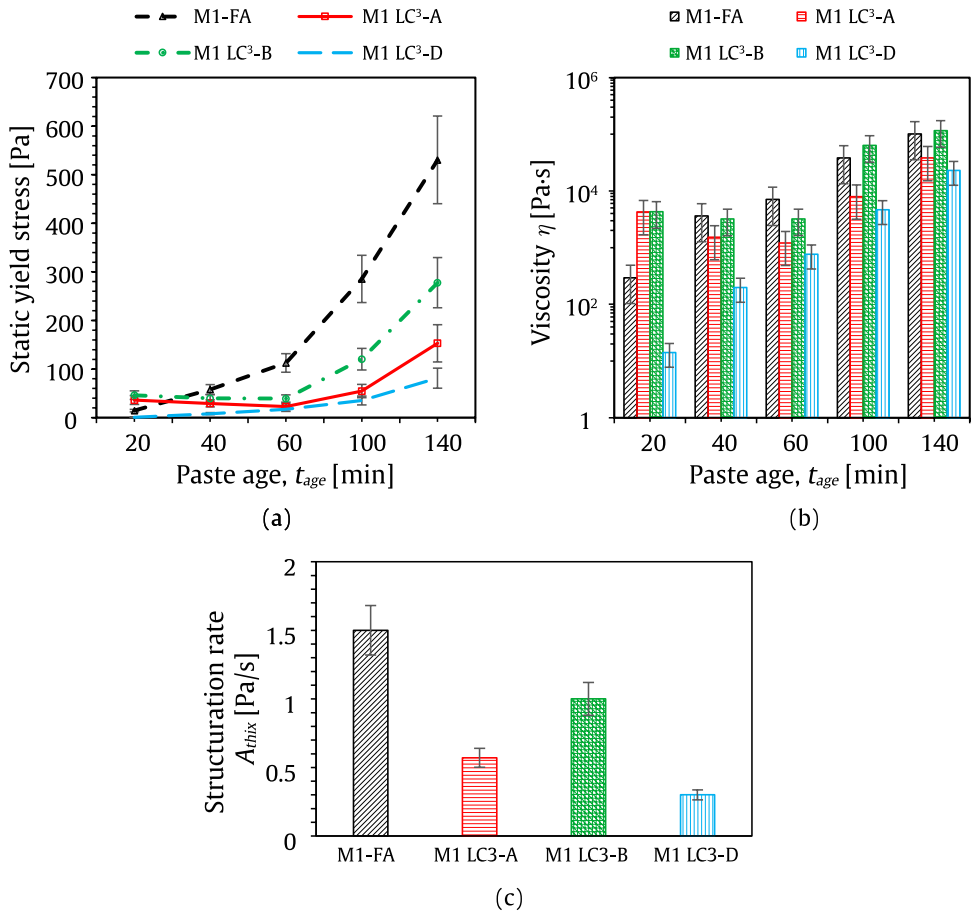

Fig. 14. (a) Static yield stress, (b) viscosity evolution over time, and (c) structuration rate parameter A_{thix} based on Perrot's model.

anhydrite (5.36 m^2/g) is also significantly higher than bassanite (1.03 m^2/g) and gypsum (1.77 m^2/g), suggesting that anhydrite-based pastes may exhibit higher water demand due to enhanced surface hydration interactions. Additionally, ettringite formation, influenced by sulfate dissolution rates (Fig. 9), can further modify the water-to-solid ratio by binding free water within its crystal structure, indirectly affecting rheology [85]. While the observed differences in rheological performance (Fig. 14) suggest possible variations in water demand among sulfate types, no direct measurements of water demand were conducted in this study. Future investigations, e.g. NMR spectroscopy, could quantitatively assess water retention and flow properties to refine the correlation between hydration kinetics, rheology, and mixing water requirements in LC^3 formulations.

Another crucial consideration derived from the stress growth tests is that the incorporation of different types of calcium sulfates can fine-tune the open times of the LC^3 binders for advanced composites. Indeed, thixotropy is known to be proportional to open time [86], and the stabilizer modifies the open time [87], while the open time affects the buildability [66]. Advanced building processes rely on a specific evolution of yield stress over time, depending on the rate at which components are built [88]. Hydration dominates in the buildup that occurs in the placed material [89]. The hydration rate after placing should remain constant throughout the whole production process to provide the same kinetics for each layer. This can be achieved by two different approaches. The first involves the continuous production of small quantities of conglomerate with high early-age strength development, such as traditional slip-forming or dry-process shotcrete, i.e., "*gunite*", and is referred to as "*controlled setting*". The second involves the continuous collection of small quantities of concrete from a larger batch and their activation with a setting activator, e.g. wet-process shotcrete, referred to as "*setting on demand*" [90,91]. These preliminary findings pave the way for future investigations and are outside the scope of the current study.

Delving into the field of 3D printing, Ibrahim et al. [38] investigated fiber-reinforced LC^3 systems and highlighted the importance of sulfate additions in stabilizing structuration and reducing deformation. Their results align with findings of the study at hand, particularly regarding the role of sulfate in controlling the thixotropic behavior. However, their study primarily employed gypsum ($CaSO_4 \cdot 2\,H_2O$) as the sulfate source which exhibited slower structuration compared to the bassanite-modified systems of the present investigation. Similarly, Chen et al. [36] confirmed that inorganic additives such as gypsum influenced the structural build-up and very early age hydration of LC^3 pastes. Increased dosages of gypsum can accelerate storage modulus G' and static yield stress evolution, increase chemically bound water and total specific surface area, which is consistent with our observations that sulfate affects structuration kinetics. Shantanu et al. [35] and Ibrahim et al. [37] further emphasized the critical role of binder-aggregate interactions in buildability. The study at hand has expanded these insights by systematically differentiating the effects of anhydrite, bassanite, and gypsum. The stress growth test results discussed in this section establish that bassanite induces the highest structuration in LC^3 pastes throughout the experiment among the three types of calcium sulfates investigated, whereas anhydrite provides a more gradual sulfate release, leading to prolonged setting and reduced early structuration.

3.3. LAOS tests

3.3.1. Linear viscoelastic region

Fig. 15 presents the development of the main rheological parameters for the M1-FA reference binder, including shear stress at the effective

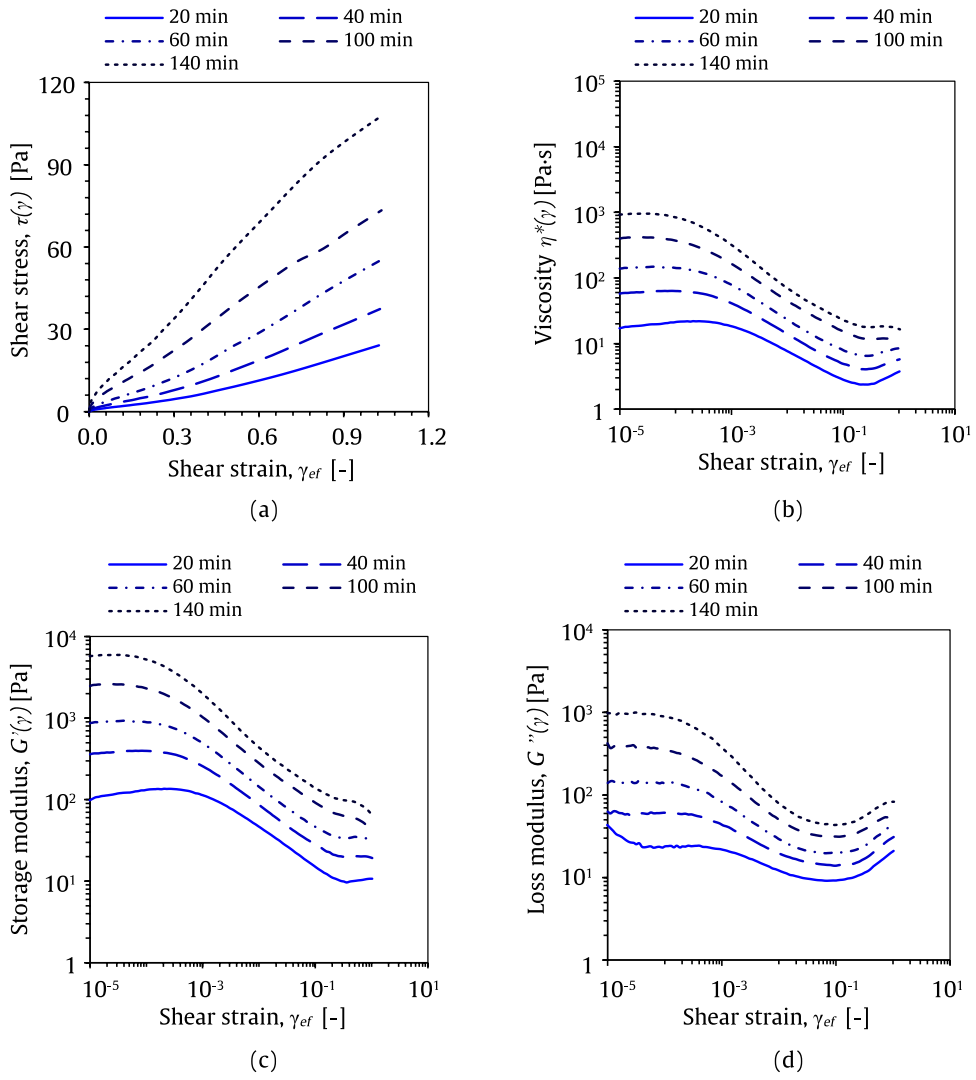

Fig. 15. (a) Shear stress, (b) complex viscosity, (c) storage modulus, and (d) loss modulus for M1-FA paste plotted against shear strain.

shear strain, complex viscosity, storage (i.e., elastic) modulus, and loss (i.e., dense) modulus. The rise in loss modulus, occurring in tandem with the cross-over strain, provides clear evidence of shear thickening. As previously suggested, this phenomenon is likely driven by adding the viscosity stabilizer. Importantly, pronounced shear-thickening may lead to a significant overestimation of the real shear stress of the paste, thereby compromising the accurate determination of process parameters critical for automated applications like robotic shotcrete and 3D printing [92–94].

Supplementary graphs can be consulted in the Appendix and present the results of the LAOS protocol applied to the three LC^3 blends. Shear stress, complex viscosity, storage modulus, and loss modulus are plotted in each figure in inlets *a*, *b*, *c*, and *d*, respectively. Due to the markedly different behavior of the tested pastes, different scales are utilized to highlight the evolution of these parameters over time, while a detailed comparison between the different pastes is provided in Fig. 16. The LC^3 pastes stiffen considerably over the test period, especially M1 LC^3-A and -B, which reach maximum stresses of 53 Pa and 102 Pa, respectively. Additionally, M1 LC^3-B outperforms M1 LC^3-A in terms of storage and loss moduli.

It is crucial to note that both M1 LC^3-A and -B pastes stiffen rapidly to the extent that measurement accuracy is affected beyond 100 minutes, as indicated by the irregular curve shapes. Given this critical evidence, the open times for these two compositions are estimated to be restricted to 90 minutes after water addition. In fact, irregularities in the LAOS curves indicate significant structuration and loss of workability and can serve as an indirect indicator of the open time, a key parameter for automated application technologies. In contrast, the relatively smooth curve observed for the M1-FA counterpart over the measured time frame of the LAOS test suggests an extended open time in excess of 140 minutes. M1 LC^3-D exhibits a markedly different rheological behavior over time, reaching a maximum shear stress of 26 Pa at a considerably later age of 140 minutes. This finding supports the conclusion drawn from the rotational rheology investigation that the slow structuration rate is attributed to calcium sulfate dihydrate. Most importantly, the three LC^3-based compositions exhibit no shear thickening. No abrupt increase in the loss modulus versus shear strain is observed, contrary to what was experienced with the benchmark M1-FA binder. This observation implies that the shear stress values and process parameters can be accurately estimated during pumping, spraying, and extruding. To facilitate a comparative analysis of the different pastes, Fig. 16 summarizes and contrasts the evolution of the rheological parameters at the boundary of the linear viscoelastic region, i.e. the first critical strain [63,71], over the paste age. The evolution of the static yield stress over time is fitted numerically using the rheological models of Roussel and Perrot [68,76]. The characteristic time t_c measured at the first critical strain for M1-FA and M1 LC^3-D is 90 minutes, whereas it is 60 minutes for M1 LC^3-A and M1 LC^3-B. This finding indicates that

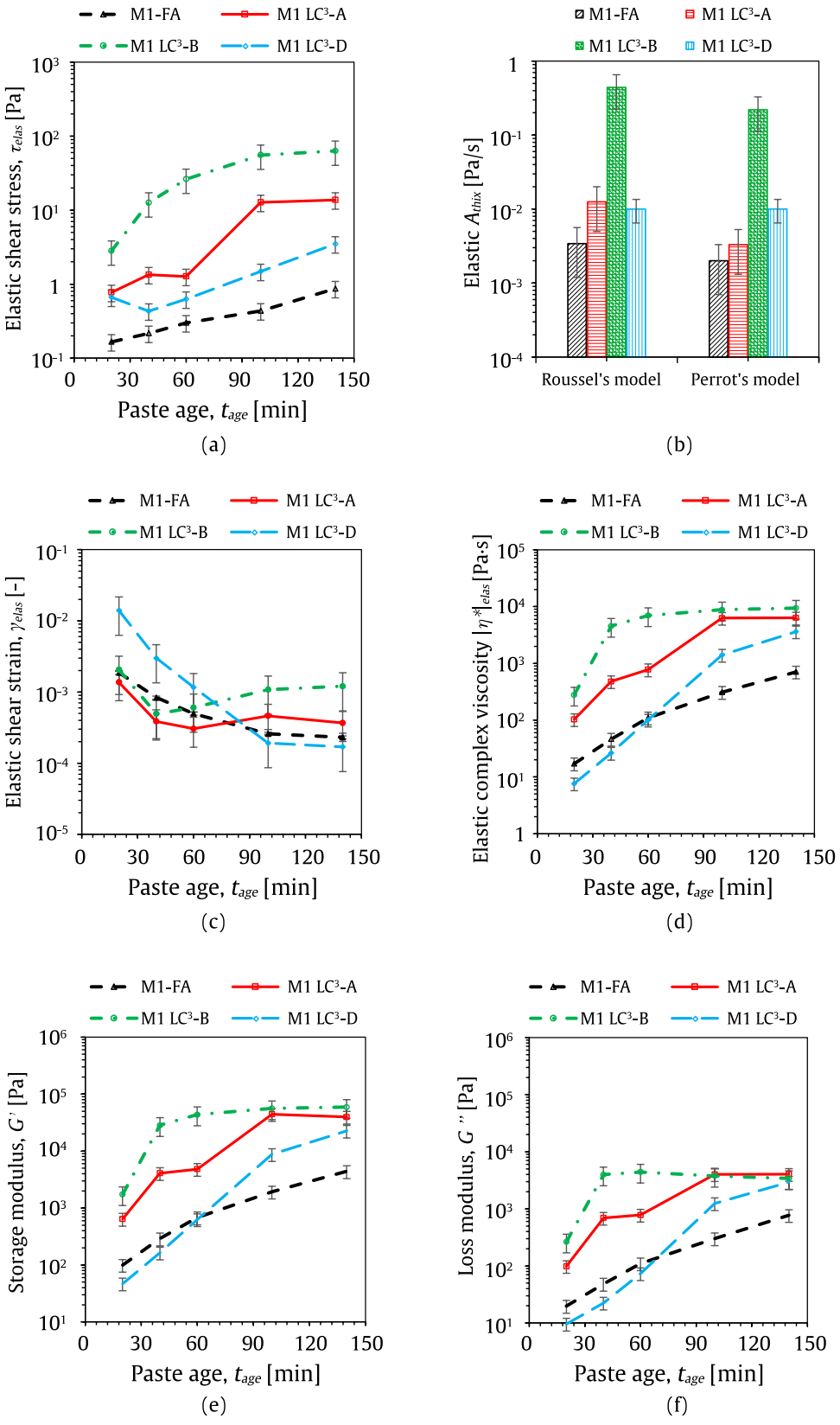

Fig. 16. Evolution of (a) elastic shear stress, (b) elastic A_{thix}, (c) elastic shear strain, (d) elastic complex viscosity, (e) storage modulus, and (f) loss modulus over the paste age.

nucleation sites become available for hydration with a slight delay in M1-FA and M1 LC^3-D, whereas M1 LC^3-A and M1 LC^3-B adhere to Perrot's model with the characteristic time at 60 minutes [68,76]. Roussel's and Perrot's models show a similar trend for A_{thix} (Fig. 16b). M1 LC^3-B exhibits the maximum structuration rate. In line with what is suggested by rotational rheometry, M1 LC^3-A shows unexpected behavior at 40 and 60 minutes. The corresponding static yield stress values fall within a narrow range, an observation consistent with storage modulus, loss modulus, complex viscosity, and shear strain data. However, the reason for this phenomenon requires further investigation. Contrary to the results of the stress growth test, the reference paste M1-FA has the lowest structuration rate and the least significant shear stress, complex viscosity, storage modulus, and loss modulus. The strain at the end of the LVR is 10^{-3}, very close to the elastic range of the mixtures. At this strain level, shearing is comparatively low. The storage modulus dominates both the loss modulus at critical strain, indicating the dominance of elastic rather than viscous behavior, and no shear thickening effect is observed. Thus, the overestimation of shear stress observed in rotational rheometry is not evident. Again, M1-FA shows a weak resistance to micro-deformation, and the critical shear stress is in good agreement with Roussel's linear structuration model.

Fig. 16a shows that M1 LC^3-B features the highest elastic yield stress at the end of the LVR, followed by M1 LC^3-A and M1 LC^3-D. The maximum critical shear strain is consistently attained by M1 LC^3-D, with the other three mixtures following within a narrow range. Roussel et al. [71] suggest that a minor critical strain may be associated with early hydrates forming preferentially at contact points. Due to a higher specific surface area, the contact points in LC^3 mixtures exceed those in M1-FA. Consequently, M1 LC^3-A and M1 LC^3-B attain critical strain at lower values than M1 LC^3-D and M1-FA mixtures. This is accompanied by higher storage modulus, loss modulus and complex viscosity.

3.3.2. Non-linear viscoelastic region

Fig. 17 plots shear stress, structuration rate (i.e., A_{thix}), complex viscosity, and shear strain about the paste age at the cross-over point, i.e., the non-linear viscoelastic region. At this stage, the flow onset of the materials is triggered, and the contribution of colloidal flocculation and thixotropy becomes dominant [71,95]. M1-FA featured the maximum cross-over shear stress, followed by M1 LC^3-B, M1 LC^3-A and M1 LC^3-D. Similarly, A_{thix} is the highest for M1-FA, with M1 LC^3-B following, according to both models used to evaluate the structuration rate. For M1 LC^3-A, the shear stress values deviate from the expected increase due to

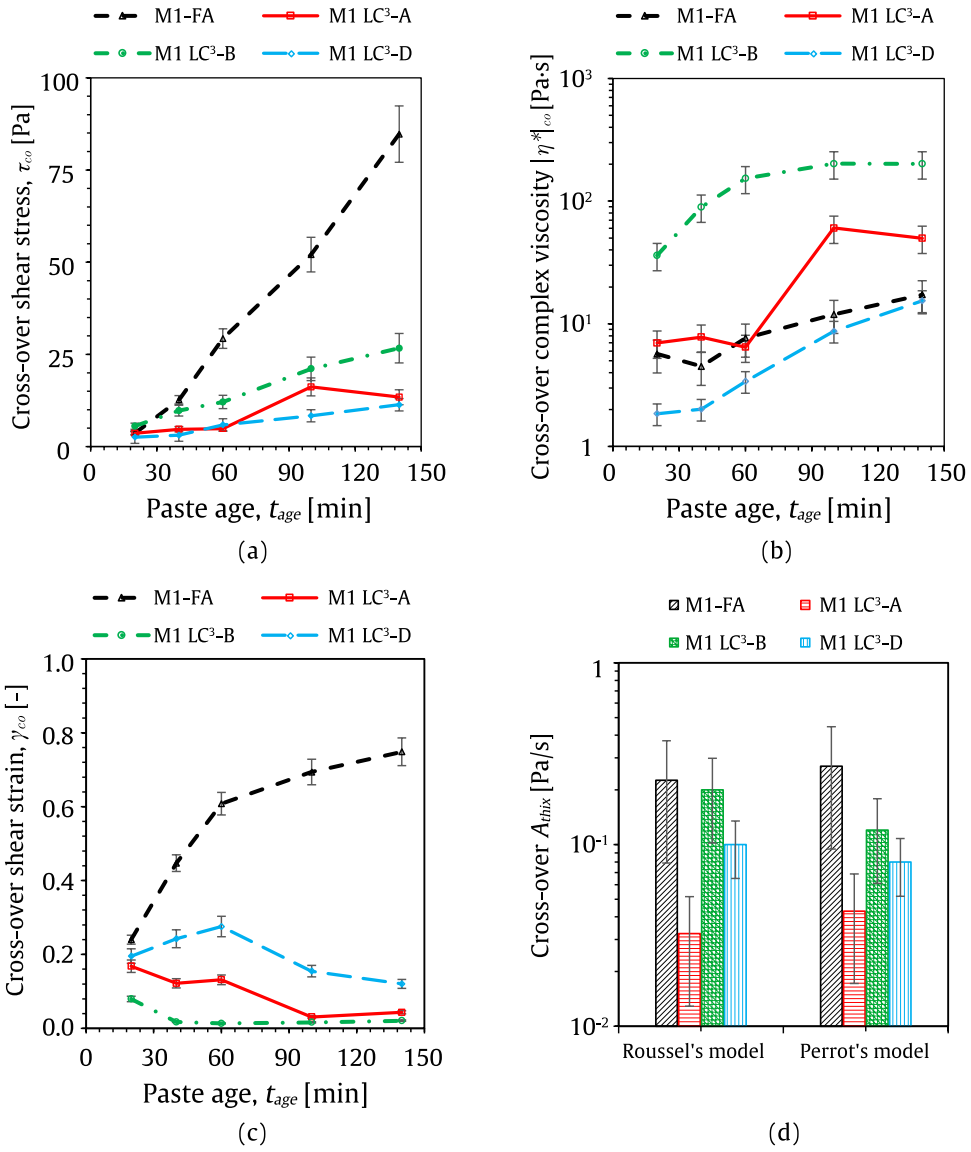

Fig. 17. Evolution of (a) shear stress, (b) complex viscosity, and (c) shear strain at the cross-over point over the paste age, and structuration rate A_{thix} according to Roussel's and Perrot's models.

the stiffness of the blend, making it difficult to effectively quantify the shear stress. The cross-over shear stress follows the same trend for LC^3 binders as suggested by rotational rheometry, being more than three times higher in the M1-FA reference paste. Again, the apparent structuration rate of M1-FA is the driving parameter at the cross-over compared to the LC^3 mixtures; unexpected behavior is observed for cross-over shear strain and complex viscosity. In fact, one might expect M1-FA to exhibit the lowest shear strain and the highest complex viscosity according to the shear stress and the structuration rate. However, the measured outcome is the opposite, highlighting an apparent incompatibility. Indeed, the risk of misleading quantification of shear stresses is a primary concern associated with the shear thickening phenomenon, as pointed out previously and substantiated here by the LAOS technique. M1 LC^3-B accounts for a negligible cross-over shear strain, lower than M1 LC^3-A and M1 LC^3-D counterparts. This sequence aligns well with the principle that minimal deformation results in maximum resistance in cementitious materials possessing higher structuration [96].

This investigation asserts that the LAOS technique is crucial for capturing the behavior of cement-based pastes, which exhibit complex rheological properties. In addition, LAOS provides accurate tools for understanding the implications of shear thickening and its impact on process parameters in key automated application technologies [46, 48–52]. From the results in the Appendix (Figs. 18–20) it can be seen that LAOS technique starts to show a significant scatter for mixtures M1 LC^3-A and M1 LC^3-B at 100 minutes and 140 minutes after water addition, unlike M1 LC^3-D. This can be owing to the workability loss due to the anhydrite and hemihydrate in comparison to the dihydrate. A similar analogy was captured by isothermal calorimetry. These artifacts should be evaluated further using the "*short amplitude oscillation technique*" to distinguish between the linear and nonlinear stress developments in the mixtures. Subsequently, the structuration rate (A_{thix}) is a critical parameter for automated construction techniques such as 3D concrete printing (3DCP) and shotcreting. In 3DCP, rapid structuration ensures layer stability by preventing deformation under the weight of subsequent layers, while excessive structuration can hinder interlayer bonding. The results in the present study show that bassanite in M1 LC^3 -B achieves a balance, with A_{thix} values of $\sim$ 0.5 Pa/min enabling sufficient open time of $\sim$ 90 min for extrusion while ensuring rapid stiffening post-deposition. This aligns with findings by Zhang et al. [86] and Chen et al. [79] who reported optimal yield stress evolution for 3DCP in the range of 200–1000 Pa. Conversely, dihydrate in M1 LC^3 -D exhibited delayed structuration, making it more suitable for applications requiring extended workability, such as slip-forming.

Holistically, the correlation between calorimetric and rheological analyses in this study provides a comprehensive understanding of the hydration kinetics and structuration mechanisms governing LC^3 binder behavior, particularly for automated construction applications like 3D concrete printing and robotic shotcrete. The isothermal calorimetry results (Fig. 9) offer critical insights into sulfate dissolution dynamics, extent of ettringite formation and early hydration rates which are directly linked to the rheological evolution captured in rotational and oscillatory rheometry. The timings and magnitudes of the hydration peaks align with rheological trends, where faster sulfate dissolution leads to accelerated structuration, impacting yield stress development and open time. For instance, the rapid dissolution of bassanite correlates with its high early structuration rate (A_{thix} $\sim$ 0.5 Pa/min), making it ideal for 3DCP, where controlled stiffening ensures interlayer stability without excessive early setting. Conversely, gypsum with its delayed sulfate availability extends workability beyond 140 minutes, benefiting robotic shotcrete applications that require prolonged pumpability before deposition. The LAOS technique further bridges calorimetry and rheology, revealing that early ettringite precipitation modifies the viscoelastic behavior, affecting both yield stress evolution and crossover strain thresholds. This multi-faceted approach underscores the necessity of synchronizing hydration kinetics with rheological tuning to optimize mixture designs for automated construction, ensuring a balance between extrudability, buildability, and workability.

4. Conclusive remarks

4.1. Summary and conclusion

This study has systematically evaluated calcium sulfate type's impact on hydration, rheology, and structuration of LC^3 binders, focusing on suitability targets for 3D printing and robotic shotcreting. This research interlinks sulfate dissolution, ettringite precipitation, and rheological structuration. Key conclusions are summarized as follows:

- The *dissolution rate* of calcium sulfate is strongly influenced by its morphology, particle size distribution (PSD), and specific surface area (SSA). *Bassanite* exhibits a rapid dissolution rate, leading to earlier ettringite formation and a higher early structuration rate, which aligns with its high suitability for layer-by-layer deposition in 3D printing. Conversely, *anhydrite* demonstrates fast dissolution despite its coarse PSD, attributable to microcracks and an increased effective surface area. *Gypsum* contributes to protracted sulfate availability, thereby delaying structuration and enhancing workability retention, a property that is advantageous for robotic shotcrete applications requiring prolonged pumpability.
- In terms of *rheological structuration* and *workability,* the structuration rate (A_{thix}) in rotational and oscillatory rheometry confirmed the key role of sulfate type on yield stress development, with bassanite-based pastes exhibiting rapid early structuration, which is crucial for enhancing buildability in 3D printing. In contrast, gypsum-based formulations retained workability for over 140 minutes, making them particularly well-suited for robotic shotcrete, where delayed stiffening is essential for efficient material transport.
- The unfavorable phenomenon of *shear thickening* was found to be severe for the binder blended with fly ash, potentially leading to nozzle clogging and inconsistent extrusion in 3D printing. On the contrary, the LC^3 -based pastes, especially those with bassanite and gypsum, showed stable viscoelastic behavior with minimal shear thickening, with positive implications for energy-efficient pumping and extrusion, as well as predictable flow behavior.
- *Water demand* was indirectly inferred from SSA and PSD of the raw constituents, relating the higher SSA of anhydrite to potential increases in water demand, whereas bassanite and gypsum, with lower SSAs, showed reduced structuration resistance. The impact of ettringite precipitation on free water availability further affected structuration and rheology, as noted in calorimetry and LAOS trends.

This study draws preliminary, albeit important, considerations for the design of LC^3 binders for advanced digitized construction technologies. Its focus has been on the selection of the appropriate calcium sulfate type. In particular, incorporating bassanite results in rapid structuration, stable viscoelastic behavior, and no severe shear thickening, making them ideal for 3D printing applications where accurate layer deposition and buildability are critical. On the other hand, adding gypsum in the LC^3 paste enables to retain workability for over 140 minutes making them suitable for shotcrete, where extended pumpability is required before deposition.

4.2. Future research perspectives

While this study provides a sound scientific basis for tailoring sulfate selection in LC^3 binders to meet the demands of emerging digital construction technologies, by integrating calorimetry, rheometry, and LAOS analysis to understand the relationship between hydration, sulfate dissolution, structuration, and rheological behavior, ongoing research shall focus on:

- Use of Portland cement clinkers instead of standardized CEM I products that already include fractions of sulfates for studying the effects of calcium sulfate species at a pure chemical-mineralogical level. Besides, various gradings of each calcium sulfate species individually could be used to overcome the seemingly contradictory SSA/PSD issues of the present study.
- Quantitative *water demand assessment* to refine correlations between SSA, hydration kinetics, and workability. In fact, hydration and rheology trends suggest strong intertwining with inherent water demand of sulfates, thus shedding more light on the impact of calcium sulfates on water retention and workability.
- Advanced microstructural studies (e.g., in-situ p-XRD, neutron scattering, or thermogravimetry) to further elucidate the role of ettringite evolution in structuration mechanisms.
- Adapting LC^3 formulations for specific digital fabrication techniques, such as continuous 3D extrusion vs. high-speed shotcreting, to maximize material efficiency and structural stability.

By addressing these aspects, LC^3 technology can further be optimized for sustainable, high-performance digital construction, offering a viable alternative to traditional cementitious materials in automated fabrication systems.

CRediT authorship contribution statement

Beigh Mirza Abdul Basit: Writing – original draft, Methodology, Investigation, Formal analysis, Data curation, Conceptualization. **Signorini Cesare:** Writing – review & editing, Visualization, Validation, Supervision, Project administration, Methodology, Formal analysis, Conceptualization. **Rauf Asim:** Investigation, Data curation. **Schröfl Christof:** Writing – review & editing, Validation, Supervision, Methodology, Conceptualization. **Köberle Thomas:** Writing – review & editing, Validation, Investigation, Data curation. **Grahl Konrad:** Investigation, Data curation. **Matschei Thomas:** Writing – review & editing, Validation, Methodology, Conceptualization. **Mechtcherine Viktor:** Writing – review & editing, Validation, Supervision, Methodology, Funding acquisition, Conceptualization.

Declaration of Competing Interest

The authors declare that they have no known competing financial interests or personal relationships that could have appeared to influence the work reported in this paper;.

Acknowledgements

The authors thank the German Research Foundation (Deutsche Forschungsgemeinschaft - DFG) for the financial support of the Research Training Group GRK 2250, project number 287321140. The authors are also grateful for the support provided by Ms. Dipl.-Krist. Ina Noack (XRD), Ms. Dipl.-Ing. Annett Willomitzer (SSA, PSD) and Mr. Christian Stahn (technical support in the laboratory).

Appendix

Linear viscoelastic region

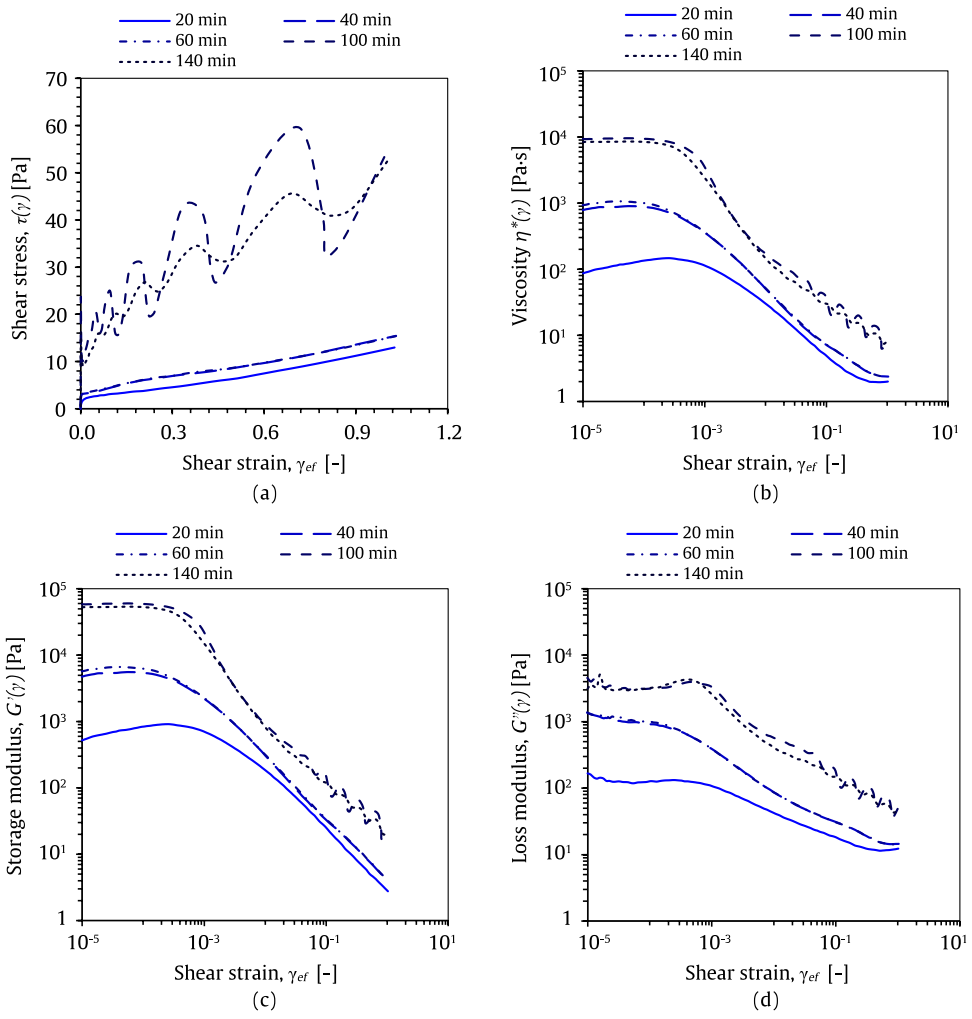

Fig. 18. (a) Shear stress, (b) complex viscosity, (c) storage modulus, and (d) loss modulus for M1 LC^3-A paste, plotted against shear strain

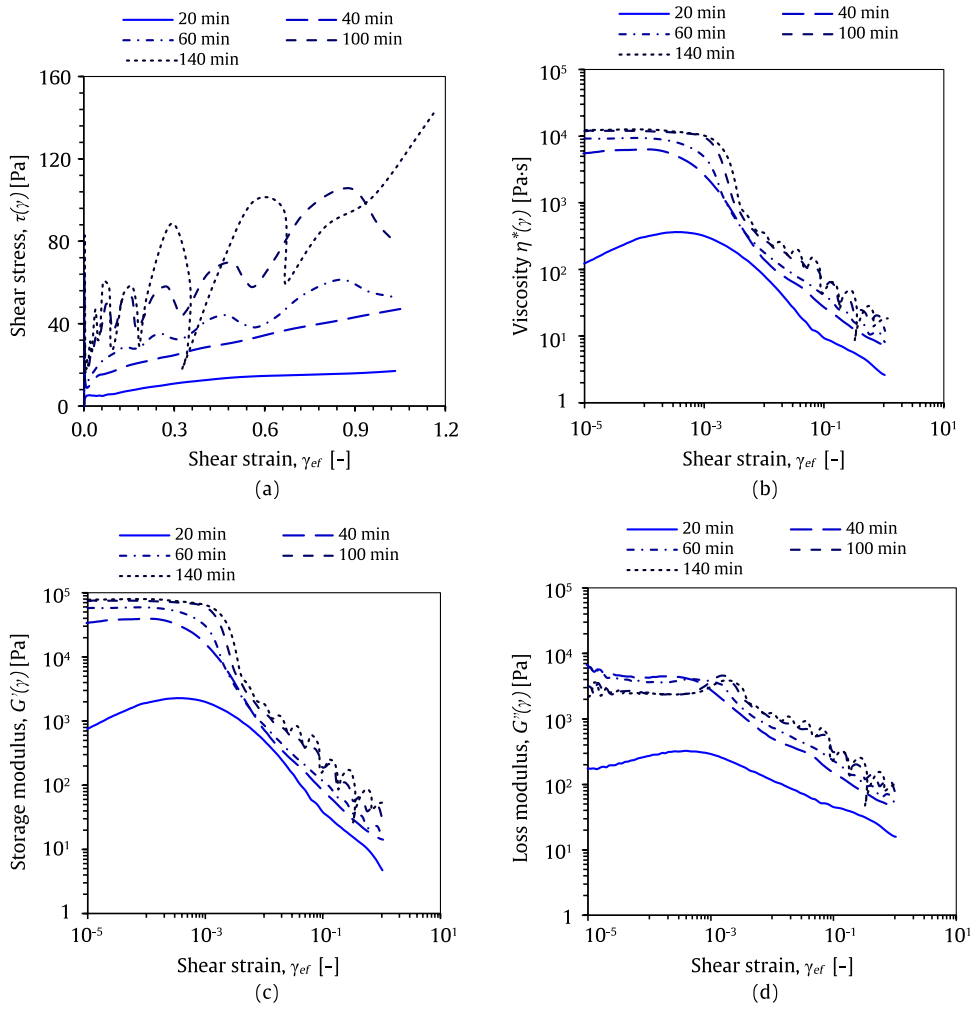

Fig. 19. (a) Shear stress, (b) complex viscosity, (c) storage modulus, and (d) loss modulus for M1 LC^3-B paste, plotted against shear strain

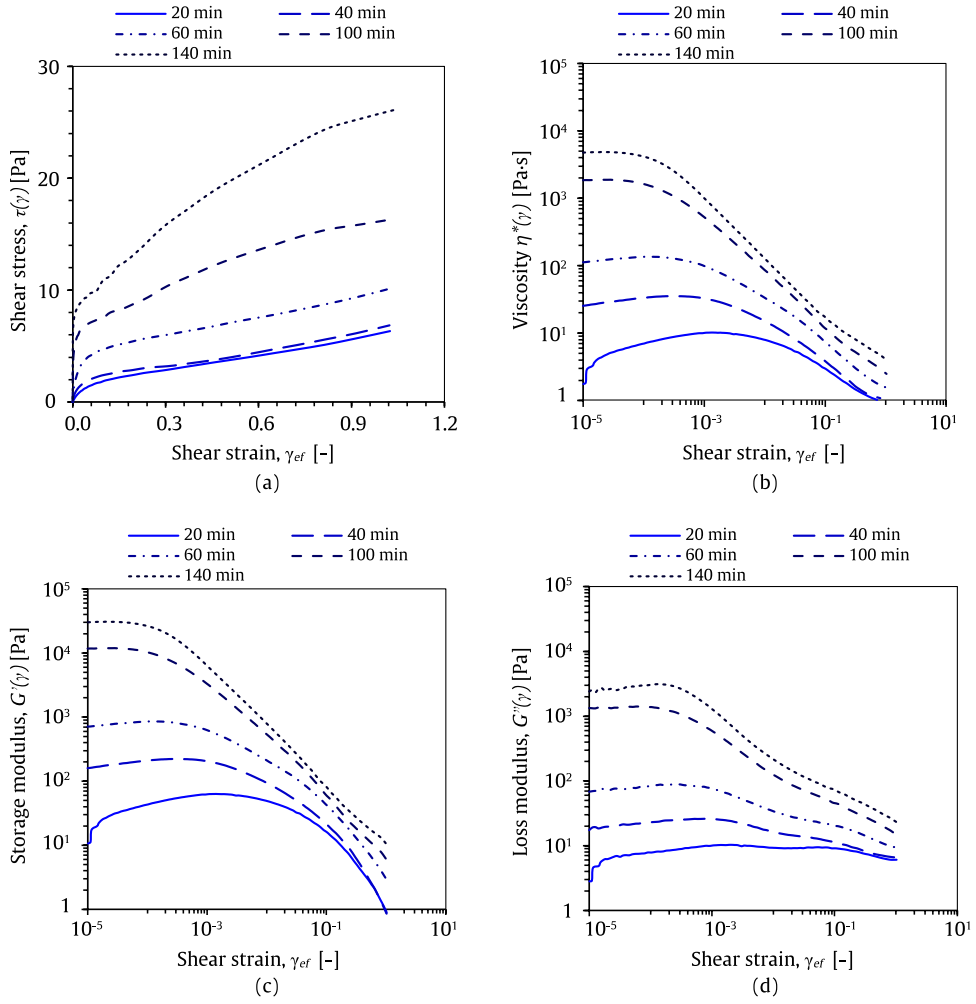

Fig. 20. (a) Shear stress, (b) complex viscosity, (c) storage modulus, and (d) loss modulus for M1 LC^3-D paste plotted against shear strain

Data Availability

Data will be made available on request.

References

[1] R. Fernandez, F. Martirena, K.L. Scrivener, The origin of the pozzolanic activity of calcined clay minerals: a comparison between kaolinite, illite and montmorillonite, Cem. Concr. Res. 41 (2011) 113–122, https://doi.org/10.1016/j.cemconres.2010.09.013.

[2] Y. Dhandapani, M. Santhanam, G. Kaladharan, S. Ramanathan, Towards ternary binders involving limestone additions — A review, Cem. Concr. Res. 143 (2021) 106396, https://doi.org/10.1016/j.cemconres.2021.106396.

[3] S.A. Miller, V.M. John, S.A. Pacca, A. Horvath, Carbon dioxide reduction potential in the global cement industry by 2050, Cem. Concr. Res. 114 (2018) 115–124, https://doi.org/10.1016/j.cemconres.2017.08.026.

[4] Y. Cancio Díaz, S. Sánchez Berriel, U. Heierli, A.R. Favier, I.R. Sánchez Machado, K. L. Scrivener, J.F. Martirena Hernández, G. Habert, Limestone calcined clay cement as a low-carbon solution to meet expanding cement demand in emerging economies, Dev. Eng. 2 (2017) 82–91, https://doi.org/10.1016/j.deveng.2017.06.001.

[5] F. Avet, R. Snellings, A. Alujas Diaz, M. Ben Haha, K. Scrivener, Development of a new rapid, relevant and reliable (R3) test method to evaluate the pozzolanic reactivity of calcined kaolinitic clays, Cem. Concr. Res. 85 (2016) 1–11, https://doi.org/10.1016/j.cemconres.2016.02.015.

[6] D. Kevin, E. Kenneth, A review of limestone additions to Portland cement and concrete, Cem. Concr. Compos 13 (1991) 165–170.

[7] K. Vance, A. Arora, G. Sant, N. Neithalath, Rheological evaluations of interground and blended cement-limestone suspensions, Constr. Build. Mater. 79 (2015) 65–72, https://doi.org/10.1016/j.conbuildmat.2014.12.054.

[8] K. Vance, A. Kumar, G. Sant, N. Neithalath, The rheological properties of ternary binders containing Portland cement, limestone, and metakaolin or fly ash, Cem. Concr. Res. 52 (2013) 196–207, https://doi.org/10.1016/j.cemconres.2013.07.007.

[9] F. Zunino, K. Scrivener, The influence of the filler effect on the sulfate requirement of blended cements, Cem. Concr. Res. 126 (2019) 105918, https://doi.org/10.1016/j.cemconres.2019.105918.

[10] M. Zajac, A. Rossberg, G. Le Saout, B. Lothenbach, Influence of limestone and anhydrite on the hydration of Portland cements, Cem. Concr. Compos 46 (2014) 99–108, https://doi.org/10.1016/j.cemconcomp.2013.11.007.

[11] K. Scrivener, A. Favier, Proceedings of the 1st International Conference on Calcined Clays for Sustainable Concrete. Calcined clays for sustainable concrete, Springer, 2015, 10.1007/978-94-017-9939-3.

[12] F. Martirena, A. Favier, K. Scrivener, Calcined Clays for Sustainable Concrete, RILEM Bookseries, 2018. https://doi.org/10.1007/978-94-024-1207-9.

[13] K. Scrivener, F. Martirena, S. Bishnoi, S. Maity, Calcined clay limestone cements (LC3), Cem. Concr. Res. (2017) 49–56, https://doi.org/10.1016/j.cemconres.2017.08.017.

[14] A.H. Ahmed, S. Nune, M. Liebscher, T. Köberle, A. Willomitzer, I. Noack, M. Butler, V. Mechtcherine, Exploring the role of dilutive effects on microstructural development and hydration kinetics of limestone calcined clay cement (LC3) made of low-grade raw materials, J. Clean. Prod. 428 (2023) 139438, https://doi.org/10.1016/j.jclepro.2023.139438.

[15] C. Signorini, F. Bracklow, M. Hering, M. Butler, L. Leicht, T. Schubert, M.A. B. Beigh, B. Beckmann, M. Curbach, V. Mechtcherine, Ballistic limit and damage assessment of hybrid fibre-reinforced cementitious thin composite plates under impact loading, J. Build. Eng. 80 (2023) 108037, https://doi.org/10.1016/j.jobe.2023.108037.

[16] C. Signorini, A. Nobili, M. Liebscher, J. Zhao, A.H. Ahmed, T. Köberle, V. Mechtcherine, Assessing the stress-transfer capability of mineral impregnated PBO yarns in a limestone calcined clay cement-based (LC3) matrix, Compos. Part B Eng. 276 (2024) 111364, https://doi.org/10.1016/j.compositesb.2024.111364.

[17] F. Avet, K. Scrivener, Investigation of the calcined kaolinite content on the hydration of Limestone Calcined Clay Cement (LC3), Cem. Concr. Res. 107 (2018) 124–135, https://doi.org/10.1016/j.cemconres.2018.02.016.
[18] F. Zunino, K. Scrivener, Reactivity and performance of limestone calcined-clay cement (lc3) Cured at Low Temperature, RILEM Book. 16 (2018) 514–520, https://doi.org/10.1007/978-94-024-1207-9_82.
[19] M. Antoni, J. Rossen, F. Martirena, K. Scrivener, Cement substitution by a combination of metakaolin and limestone, Cem. Concr. Res. 42 (2012) 1579–1589, https://doi.org/10.1016/j.cemconres.2012.09.006.
[20] Y. Dhandapani, M. Santhanam, Investigation on the microstructure-related characteristics to elucidate performance of composite cement with limestone-calcined clay combination, Cem. Concr. Res. 129 (2020) 105959, https://doi.org/10.1016/j.cemconres.2019.105959.
[21] K. Scrivener, F. Avet, H. Maraghechi, F. Zunino, J. Ston, W. Hanpongpun, A. Favier, Impacting factors and properties of limestone calcined clay cements (LC3, Green. Mater. 7 (2018) 3–14, https://doi.org/10.1680/jgrma.18.00029.
[22] A.P. Kirchheim, V. Fernàndez-Altable, P.J.M. Monteiro, D.C.C. Dal Molin, I. Casanova, Analysis of cubic and orthorhombic C3A hydration in presence of gypsum and lime, J. Mater. Sci. 44 (2009) 2038–2045, https://doi.org/10.1007/s10853-009-3292-3.
[23] A. Quennoz, K.L. Scrivener, Interactions between alite and C3A-gypsum hydrations in model cements, Cem. Concr. Res. 44 (2013) 46–54, https://doi.org/10.1016/j.cemconres.2012.10.018.
[24] I. De la Varga, J. Castro, D.P. Bentz, F. Zunino, J. Weiss, Evaluating the hydration of high volume fly ash mixtures using chemically inert fillers, Constr. Build. Mater. 161 (2018) 221–228, https://doi.org/10.1016/j.conbuildmat.2017.11.132.
[25] M.D. Niemuth, L. Barcelo, J. Weiss, Effect of fly ash on optimum sulfate levels measured using heat and strength at early ages, Adv. Civ. Eng. Mater. 1 (2012), https://doi.org/10.1520/acem20120012.
[26] M.D. Effect of Fly Ash on Optimum Sulfate of Portland Cement, Purdue University, 2012 https://doi.org/10.1016/s0008-8846(99)00153-2.
[27] S. Krishnan, A.C. Emmanuel, S. Bishnoi, Hydration and phase assemblage of ternary cements with calcined clay and limestone, Constr. Build. Mater. 222 (2019) 64–72, https://doi.org/10.1016/j.conbuildmat.2019.06.123.
[28] W. Lerch, The influence of gypsum on the hydration and properties of portland cement pastes, Acids Spec. Publ. 249 (2008).
[29] F.A.Zunino Sommariva, Limestone calcined clay cements (LC3): raw material processing, sulfate balance and hydration kinetics, 2020.
[30] F. Zunino, K. Scrivener, Microstructural developments of limestone calcined clay cement (LC3) pastes after long-term (3 years) hydration, Cem. Concr. Res. 153 (2022), https://doi.org/10.1016/j.cemconres.2021.106693.
[31] H. Minard, S. Garrault, L. Regnaud, A. Nonat, Mechanisms and parameters controlling the tricalcium aluminate reactivity in the presence of gypsum, Cem. Concr. Res. 37 (2007) 1418–1426, https://doi.org/10.1016/j.cemconres.2007.06.001.
[32] R. Myers, G. Geng, J. Li, E. Rodríguez, J. Ha, P. Kidkhunthod, G. Sposito, L. Lammers, A. Kirchheim, P. Monteiro, Role of adsorption phenomena in cubic tricalcium aluminate dissolution, Langmuir 22 (2017) 45–55, https://doi.org/doi:10.1021/acs.langmuir.6b03474.
[33] G. Geng, R.J. Myers, Y.S. Yu, D.A. Shapiro, R. Winarski, P.E. Levitz, D.A. L. Kilcoyne, P.J.M. Monteiro, Synchrotron X-ray nanotomographic and spectromicroscopic study of the tricalcium aluminate hydration in the presence of gypsum, Cem. Concr. Res. 111 (2018) 130–137, https://doi.org/10.1016/j.cemconres.2018.06.002.
[34] F. Zunino, K. Scrivener, The reaction between metakaolin and limestone and its effect in porosity refinement and mechanical properties, Cem. Concr. Res. 140 (2021) 106307, https://doi.org/10.1016/j.cemconres.2020.106307.
[35] B. Shantanu, J. Smrati, S. Manu, Criticality of binder-aggregate interaction for buildability of 3D printed concrete containing limestone calcined clay, Cem. Concr. Compos 136 (2023) 104853, https://doi.org/10.1016/j.cemconcomp.2022.104853.
[36] Y. Chen, Y. Zhang, S. He, X. Liang, E. Schlangen, O. Çopuroğlu, Improving structural build-up of limestone-calcined clay-cement pastes by using inorganic additives, Constr. Build. Mater. 392 (2023) 131959, https://doi.org/10.1016/j.conbuildmat.2023.131959.
[37] K.A. Ibrahim, G.P.A.G. Van Zijl, A.J. Babafemi, Comparative studies of LC3- and fly ash-based blended binders in fibre-reinforced printed concrete (FRPC): Rheological and quasi-static mechanical characteristics, J. Build. Eng. 80 (2023) 108016, https://doi.org/10.1016/j.jobe.2023.108016.
[38] K.A. Ibrahim, G.P.A.G. Van Zijl, A.J. Babafemi, Mitigation of lack of fusion in 3D printed limestone calcined clay cement concrete induced by effective microorganisms, Case Stud. Constr. Mater. 20 (2024) e03176, https://doi.org/10.1016/j.cscm.2024.e03176.
[39] P.F.G. Banfill, Rheology of fresh cement and concrete, Rheol. Rev. Br. Soc. Rheol. (2006) 61–130.
[40] R.J. Flatt, Towards a prediction of superplasticized concrete rheology, Mater. Struct. 37 (2004) 289–300, https://doi.org/10.1007/bf02481674.
[41] H. Ding, X. Shen, A. Chen, R. Gu, Y. Fang, D. Li, Study on the effect of three types of calcium sulfate on the early hydration and workability of self-compacting repair mortar, Materials 16 (2023) 5648, https://doi.org/10.3390/ma16165648.
[42] J.S. Andrade Neto, P.R. De Matos, A.G. De La Torre, C.E.M. Campos, P.J.P. Gleize, P.J.M. Monteiro, A.P. Kirchheim, The role of sodium and sulfate sources on the rheology and hydration of C3A polymorphs, Cem. Concr. Res. 151 (2022) 106639, https://doi.org/10.1016/j.cemconres.2021.106639.
[43] J. Dong, H. Wu, S. Xie, X. Shang, Z. Shi, Z. Tu, P. Zhou, T. Zhang, Impact of calcium formate and anhydrous sodium sulfate on the flowability, mechanical properties, and hydration characteristics of UHPC, J. Build. Eng. 96 (2024) 110534, https://doi.org/10.1016/j.jobe.2024.110534.
[44] M. Sharma, S. Bishnoi, F. Martirena, K. Scrivener, Limestone calcined clay cement and concrete: a state-of-the-art review, Cem. Concr. Res. 149 (2021) 106564, https://doi.org/10.1016/j.cemconres.2021.106564.
[45] F. Zunino, Y. Dhandapani, M. Ben Haha, J. Skibsted, S. Joseph, S. Krishnan, A. Parashar, M.C.G. Juenger, T. Hanein, S.A. Bernal, K.L. Scrivener, F. Avet, Hydration and mixture design of calcined clay blended cements: review by the RILEM TC 282-CCL, Mater. Struct. Constr. 55 (2022), https://doi.org/10.1617/s11527-022-02060-1.
[46] T.R. Muzenda, P. Hou, S. Kawashima, T. Sui, X. Cheng, The role of limestone and calcined clay on the rheological properties of LC3, Cem. Concr. Compos 107 (2020) 103516, https://doi.org/10.1016/j.cemconcomp.2020.103516.
[47] S. Ferreiro, D. Herfort, J.S. Damtoft, Effect of raw clay type, fineness, water-to-cement ratio and fly ash addition on workability and strength performance of calcined clay – Limestone Portland cements, Cem. Concr. Res. 101 (2017) 1–12, https://doi.org/10.1016/j.cemconres.2017.08.003.
[48] M. Chen, H. Li, L. Yang, S. Wang, P. Zhao, Y. Huang, L. Lu, G. Yue, Q. Li, Rheology and shape stability control of 3D printed calcium sulphoaluminate cement composites containing paper milling sludge, Addit. Manuf. 54 (2022), https://doi.org/10.1016/j.addma.2022.102781.
[49] T. Conte, M. Chaouche, Rheological behavior of cement pastes under large amplitude oscillatory shear, Cem. Concr. Res. 89 (2016) 332–344, https://doi.org/10.1016/j.cemconres.2016.07.014.
[50] T. Conte, M. Chaouche, Parallel superposition rheology of cement pastes, Cem. Concr. Compos 104 (2019) 103393, https://doi.org/10.1016/j.cemconcomp.2019.103393.
[51] P. Hou, T.R. Muzenda, Q. Li, H. Chen, S. Kawashima, T. Sui, H. Yong, N. Xie, X. Cheng, Mechanisms dominating thixotropy in limestone calcined clay cement (LC3), Cem. Concr. Res. 140 (2021) 106316, https://doi.org/10.1016/j.cemconres.2020.106316.
[52] J. Cui, Z. He, G. Zhang, X. Cai, Rheological properties of sprayable ultra-high performance concrete with different viscosity-enhancing agents, Construction and Building Materials, Constr. Build. Mater. 321 (2022), https://doi.org/10.1016/j.conbuildmat.2021.126154.
[53] T. Gong, Tensile behavior of high-performance cement-based composites with hybrid reinforcement subjected to quasi-static and impact loading, Tech. Univ. ät Dresd. (2021).
[54] M.A.B. Beigh, V.N. Nerella, C. Schröfl, V. Mechtcherine, Studying the Rheological Behavior of Limestone Calcined Clay Cement (LC3) Mixtures in the Context of Extrusion-Based 3D-Printing, Springer Singapore, 2020, https://doi.org/10.1007/978-981-15-2806-4_26.
[55] F. Zunino, K. Scrivener, Factors influencing the sulfate balance in pure phase C3S/C3A systems, Cem. Concr. Res. 133 (2020) 106085, https://doi.org/10.1016/j.cemconres.2020.106085.
[56] L. Wang, N. Ur Rehman, I. Curosu, Z. Zhu, M.A.B. Beigh, M. Liebscher, L. Chen, D. C.W. Tsang, S. Hempel, V. Mechtcherine, On the use of limestone calcined clay cement (LC3) in high-strength strain-hardening cement-based composites (HS-SHCC), Cem. Concr. Res. 144 (2021) 106421, https://doi.org/10.1016/j.cemconres.2021.106421.
[57] C. Signorini, A.H. Ahmed, M. Liebscher, J. Zhao, T. Köberle, V. Mechtcherine, Hybrid fibre-reinforced cementitious composites with short polyethylene and continue carbon fibres: influence of roving impregnation on tensile and cracking behaviour, Mater. Des. 248 (2024) 113465, https://doi.org/10.1016/j.matdes.2024.113465.
[58] F. Bracklow, C.M. Jackson, C. Signorini, E. Jacques, B. Beckmann, M. Curbach, V. Mechtcherine, Hybrid mineral-bonded protective layers for enhanced self-centering capacity of reinforced concrete beams subjected to blast, Eng. Struct. 322 (2025) 119151, https://doi.org/10.1016/j.engstruct.2024.119151.
[59] S. Mantellato, M. Palacios, R.J. Flatt, Relating early hydration, specific surface and flow loss of cement pastes, Mater. Struct. Constr. 52 (2019), https://doi.org/10.1617/s11527-018-1304-y.
[60] S. Mantellato, M. Palacios, R.J. Flatt, Reliable specific surface area measurements on anhydrous cements, Cem. Concr. Res. 67 (2015) 286–291, https://doi.org/10.1016/j.cemconres.2014.10.009.
[61] I. Mehdipour, K.H. Khayat, Effect of Particle-size Distribution and Specific Surface Area of Different Binder Systems on Packing Density and Flow Characteristics of Cement paste, Elsevier Ltd, 2017, 10.1016/j.cemconcomp.2017.01.005.
[62] R. Cepuritis, S. Jacobsen, S. Smeplass, E. Mørtsell, B.J. Wigum, S. Ng, Influence of crushed aggregate fines with micro-proportioned particle size distributions on rheology of cement paste, Cem. Concr. Compos 80 (2017) 64–79, https://doi.org/10.1016/j.cemconcomp.2017.02.012.
[63] N. Roussel, A thixotropy model for fresh fluid concretes: Theory, validation and applications, Cem. Concr. Res. 36 (2006) 1797–1806, https://doi.org/10.1016/j.cemconres.2006.05.025.
[64] V.N. Nerella, M.A.B. Beigh, S. Fataei, V. Mechtcherine, Strain-based approach for measuring structural build-up of cement pastes in the context of digital construction, Cem. Concr. Res. 115 (2019) 530–544, https://doi.org/10.1016/j.cemconres.2018.08.003.
[65] I. Ivanova, V. Mechtcherine, Possibilities and challenges of constant shear rate test for evaluation of structural build-up rate of cementitious materials, Cem. Concr. Res. 130 (2020) 105974, https://doi.org/10.1016/j.cemconres.2020.105974.
[66] A. Perrot, D. Rangeard, A. Pierre, Structural built-up of cement-based materials used for 3D-printing extrusion techniques, Mater. Struct. Constr. 49 (2015) 1213–1220, https://doi.org/10.1617/s11527-015-0571-0.

[67] D.C.H. Cheng, F. Evans, Phenomenological characterization of the rheological behaviour of inelastic reversible thixotropic and antithixotropic fluids, Br. J. Appl. Phys. 16 (1965) 1599–1617, https://doi.org/10.1088/0508-3443/16/11/301.
[68] N. Roussel, Steady and transient flow behaviour of fresh cement pastes, Cem. Concr. Res. 35 (2005) 1656–1664, https://doi.org/10.1016/j.cemconres.2004.08.001.
[69] I. Ivanova, V. Mechtcherine, Effects of volume fraction and surface area of aggregates on the static yield stress and structural build-up of fresh concrete, Materials 13 (2020), https://doi.org/10.3390/ma13071551.
[70] J.J. Stickel, J.S. Knutsen, M.W. Liberatore, Connecting large amplitude oscillatory shear rheology to unidirectional shear rheology and application to biomass slurries, Appl. Rheol. 24 (2014), https://doi.org/10.3933/APPLRHEOL-24-53075.
[71] N. Roussel, G. Ovarlez, S. Garrault, C. Brumaud, The origins of thixotropy of fresh cement pastes, Cem. Concr. Res. 42 (2012) 148–157, https://doi.org/10.1016/j.cemconres.2011.09.004.
[72] K. Hyun, M. Wilhelm, C.O. Klein, K.S. Cho, J.G. Nam, K.H. Ahn, S.J. Lee, R. H. Ewoldt, G.H. McKinley, A review of nonlinear oscillatory shear tests: Analysis and application of large amplitude oscillatory shear (LAOS), Prog. Polym. Sci. Oxf. 36 (2011) 1697–1753, https://doi.org/10.1016/j.progpolymsci.2011.02.002.
[73] R.H. Ewoldt, Defining nonlinear rheological material functions for oscillatory shear, J. Rheol. 57 (2013) 177–195, https://doi.org/10.1122/1.4764498.
[74] H. Randy, S.B. Heidelberg, C.C.A. Alike, A. Published, D. Terms, Mapping thixo-elasto-visco-plastic behavior, (2017) 0–39..
[75] R.H. Ewoldt, A.E. Hosoi, G.H. McKinley, New measures for characterizing nonlinear viscoelasticity in large amplitude oscillatory shear, J. Rheol. 52 (2008) 1427–1458, https://doi.org/10.1122/1.2970095.
[76] A. Perrot, D. Rangeard, A. Pierre, Structural built-up of cement-based materials used for 3D- printing extrusion techniques, Mater. Struct. Constr. 49 (2015) 1213–1220, https://doi.org/10.1617/s11527-015-0571-0.
[77] C. Rodriguez, J.I. Tobon, Influence of calcined clay/limestone, sulfate and clinker proportions on cement performance, Constr. Build. Mater. 251 (2020) 119050, https://doi.org/10.1016/j.conbuildmat.2020.119050.
[78] K. Scrivener, F. Avet, H. Maraghechi, F. Zunino, J. Ston, W. Hanpongpun, A. Favier, Impacting factors and properties of limestone calcined clay cements (LC3, Green. Mater. 7 (2018) 3–14, https://doi.org/10.1680/jgrma.18.00029.
[79] Y. Chen, Y. Zhang, B. Šavija, O. Çopuroğlu, Fresh properties of limestone-calcined clay-slag cement pastes, Cem. Concr. Compos 138 (2023), https://doi.org/10.1016/j.cemconcomp.2023.104962.
[80] K.E. Atkinson, An Introduction to Numerical Analysis, John Wiley & Sons, 1989.
[81] R.K. Mishra, K. Kanhaiya, J.J. Winetrout, R.J. Flatt, H. Heinz, Force field for calcium sulfate minerals to predict structural, hydration, and interfacial properties, Cem. Concr. Res. 139 (2021) 106262, https://doi.org/10.1016/j.cemconres.2020.106262.
[82] H. Pöllmann, in: Cementitious Materials: Composition, Properties, Application, De Gruyter, 2017, https://doi.org/10.1515/9783110473728.
[83] C. Jakob, D. Jansen, J. Dengler, J. Neubauer, Controlling ettringite precipitation and rheological behavior in ordinary Portland cement paste by hydration control agent, temperature and mixing, Cem. Concr. Res. 166 (2023) 107095, https://doi.org/10.1016/j.cemconres.2023.107095.
[84] C. Jakob, D. Jansen, N. Ukrainczyk, E. Koenders, U. Pott, D. Stephan, J. Neubauer, Relating ettringite formation and rheological changes during the initial cement hydration, Materials (2019).
[85] B. Lothenbach, T. Matschei, G. Möschner, F.P. Glasser, Thermodynamic modelling of the effect of temperature on the hydration and porosity of Portland cement, Cem. Concr. Res. 38 (2008) 1–18, https://doi.org/10.1016/j.cemconres.2007.08.017.
[86] Y. Zhang, Y. Zhang, W. She, L. Yang, G. Liu, Y. Yang, Rheological and harden properties of the high-thixotropy 3D printing concrete, Constr. Build. Mater. 201 (2019) 278–285, https://doi.org/10.1016/j.conbuildmat.2018.12.061.
[87] Y. Chen, S.C. Figueiredo, Ç . Yalçinkaya, O. Çopuroğlu, F. Veer, E. Schlangen, The effect of viscosity-modifying admixture on the extrudability of limestone and calcined clay-based cementitious material for extrusion-based 3D concrete printing, Materials 12 (2019) 9–12, https://doi.org/10.3390/ma12091374.
[88] V.N. 1988- Nerella, Technische Universität Dresden, Development and characterisation of cement-based materials for extrusion-based 3D-printing = Entwicklung und Charakterisierung von zementgebundenen Baustoffen für den extrusion-based 3D-printing, 2019.
[89] V.N. Nerella, M.A.B. Beigh, S. Fataei, V. Mechtcherine, Strain-based approach for measuring structural build-up of cement pastes in the context of digital construction, Cem. Concr. Res. 115 (2019) 530–544, https://doi.org/10.1016/j.cemconres.2018.08.003.
[90] L. Reiter, T. Wangler, A. Anton, R.J. Flatt, Setting on demand for digital concrete – Principles, measurements, chemistry, validation, Cem. Concr. Res. 132 (2020) 106047, https://doi.org/10.1016/j.cemconres.2020.106047.
[91] L. Reiter, T. Wangler, N. Roussel, R.J. Flatt, The role of early age structural build-up in digital fabrication with concrete, Cem. Concr. Res. 112 (2018) 86–95, https://doi.org/10.1016/j.cemconres.2018.05.011.
[92] M. Li, J. Han, Y. Zhou, P. Yan, A rheological model for evaluating the behavior of shear thickening of highly Flowable mortar, Molecules 26 (2021), https://doi.org/10.3390/molecules26041011.
[93] L. Yang, H. Wang, A. Wu, H. Li, A.B. Tchamba, T.A. Bier, Shear thinning and thickening of cemented paste backfill, Appl. Rheol. 29 (2019) 80–93, https://doi.org/10.1515/ARH-2019-0008.
[94] Y. Chen, S. He, Y. Zhang, Z. Wan, O. Çopuroğlu, E. Schlangen, 3D printing of calcined clay-limestone-based cementitious materials, Cem. Concr. Res. 149 (2021), https://doi.org/10.1016/j.cemconres.2021.106553.
[95] Y. Qian, S. Ma, S. Kawashima, G. De Schutter, Rheological characterization of the viscoelastic solid-like properties of fresh cement pastes with nanoclay addition, Theor. Appl. Fract. Mech. (2019) 102262, https://doi.org/10.1016/j.tafmec.2019.102262.
[96] I. Mehdipour, K.H. Khayat, Understanding the role of particle packing characteristics in rheo-physical properties of cementitious suspensions: a literature review, Constr. Build. Mater. 161 (2018) 340–353, https://doi.org/10.1016/j.conbuildmat.2017.11.147.